Mon. Not. R. astr. Soc. (1982) **198**, 483–516

Atmospheric kinematics of high velocity long period variables

L. A. Willson *Erwin Fick Observatory, Iowa State University, Ames, Iowa 50011, USA*

G. Wallerstein* and C. A. Pilachowski† *University of Washington, Seattle, Washington 98195 USA*

Received 1981 March 26; in original form 1980 December 9

Summary. We have analysed radial velocities of atomic absorption lines of three long period variables, RT Cyg, Z Oph and S Car, in order to understand velocity gradients and discontinuities in their atmospheres. Phase coverage is from five days before maximum to 73 days after maximum for RT Cyg, from 17 days before to 44 days after maximum for Z Oph, and at 9 days before maximum for S Car.

On a few spectrograms double lines were seen. All spectrograms were analysed by a four-parameter regression programme to yield the dependence of the radial velocity on the excitation potential, first ionization potential, wavelength and line strength, as indicators of the depth of line formation.

The data were analysed to yield the velocity discontinuity across shock waves and velocity gradients between shock waves. Near maximum light the radial velocities cannot be understood by the presence of one shock only but rather require two shocks. The lower shock becomes apparent at the longer wavelengths and has already been recognized in other long period variables whose spectra have been observed at high resolution in the 2-μm region. Our ability to see more deeply into the atmospheres of long period variables at long wavelengths indicates that the opacity decreases rapidly with wavelength. This is probably due to the importance of Rayleigh scattering as an opacity source.

Consistent parameters are obtained if these stars are fundamental mode pulsators with total masses in the range of $0.5-1.0 M_{\odot}$ and effective radii in the range of $0.85-1.5 \times 10^{13}$ cm.

* 1980–1981 Visiting Fellow, Joint Institute for Laboratory Astrophysics, National Bureau of Standards and University of Colorado, Boulder, Colorado, USA.

† Present address: Kitt Peak National Observatory, Tucson, Arizona, USA.

1 Introduction

Apart possibly from supernovae of type I the bolometrically brightest stars of Population II are the long period variables such as are found in the globular cluster 47 Tuc and the elliptical galaxies near the Andromeda nebula (Baade 1963). Since they are extremely rare in loose ellipticals (such as the systems in Sculptor and Draco) or the more metal-poor globulars, the long period variables of Population II probably have intermediate metal content and should be classified as belonging to the old disc population (Feast 1962). Their great brightness, especially in the near infrared, makes them accessible targets for abundance analysis once their atmospheres can be sufficiently understood.

The atmospheres of long period variables show substantial deviations from standard non-variable atmospheres, especially near light maximum when emission lines of hydrogen and other elements emerge and double absorption lines are sometimes seen (Wing 1979). While such phenomena present substantial obstacles to abundance analyses, they also present opportunities to investigate the physical processes responsible for the emission spectrum seen at maximum and post-maximum phases of the cycle. The interpretation of these phenomena as due to a shock wave in the stellar atmosphere was first suggested by Merrill (1940). The doubling of absorption lines is additional evidence for the presence of a shock wave, with one component presumably being formed in front of the shock and the second component being formed behind the shock. Such double lines were first seen in the long period variable R And by Merrill & Greenstein (1958) and were first related to a complete velocity curve by Maehara (1968) for χ Cyg. Recently, observations in the near infrared with Fourier transform spectrometers have revealed double lines in many long period variables (Hinkle 1978; Hinkle & Barnes 1979; Hall, Hinkle & Ridgway 1979).

While double absorption lines seem to be easy to detect at wavelengths greater than about 8000 Å, the increasing opacity at shorter λ (due to Rayleigh scattering) seems to be the reason that double lines have not generally been visible in the commonly observed violet region of the spectrum even with very high spectral resolution. Stars of spectral type M5 and later cannot be observed for atomic lines between about λ 8000 and λ 4400 because of extensive blanketing by TiO bands. Some of the shorter period stars, especially those of high velocity, have weak TiO absorption at maximum and their atomic lines can be measured throughout much of the spectrum. Near minimum light, however, this opportunity is lost as TiO absorption strengthens and the stars become too faint for high resolution data. Hence we have been conducting a programme of visual observation and data analysis for three stars, RT Cyg (P = 190 day), Z Oph (P = 349 day) and S Car (P = 150 day) near light maximum.

For RT Cyg, we have been assembling spectra taken near maximum for 6 yr. In addition we have measured plates of RT Cyg and Z Oph from the Hale Observatory files and have observed S Car on one occasion. Since there is always some chance that our results will depend partially or even completely upon our method of analysis (Eddington 1939) we should describe our data reduction methods. All spectrograms were measured with an oscilloscope measuring engine of the Grant type. The reduction program yields wavelengths for the stellar lines which are identified using standard lists such as that of Davis (1947). An approximate radial velocity from earlier measurements had to be assumed or else the number of possible candidates for each identification would be hopelessly large. No exact limits were set around the assumed velocity, and rarely is a reasonable identification found with a deviation of more than 15 km s^{-1} for more than a few lines on any spectrogram. A master list of likely lines was then assembled and final identification was accomplished by the CDC 6400 computer from the master list and specified velocity interval. The latter ranged from $\pm$13 km s^{-1} for plates that showed no velocity gradient or evidence of line doubling to $\pm$23 km s^{-1} for spectrograms that showed doubling or strong gradients. In the latter situation some lines that

were close together had to be eliminated. Our list of standard lines for the wavelength interval λλ 3700–7000 Å is available upon request.

After a radial velocity was calculated for each line we plotted histograms of the velocity distribution for each spectrogram and also investigated the dependence of velocity upon excitation potential, wavelength, ionization potential, and line strength by a multiple regression technique as described by Pilaschowski, Wallerstein & Willson (1979, hereafter PWW). At times the regression analysis indicated that line doubling was likely to be present, and that a remeasurement of the plate was in order. Such remeasurements are reported here, as are measurements of two more plates of RT Cyg taken at and after light maximum in 1978, one plate of RT Cyg from the Hale Observatory files taken near maximum light, and recent identifications and velocities for TiO rotational lines. In Section 3 we describe the methods and assumptions in detail; in Sections 4–6 we present our data for the three variable stars RT Cyg, Z Oph and S Car, and discuss the implications of the results for each star in terms of the shock wave model of Hill & Willson (1979, hereafter HW).

2 Data and reductions

Our spectrograms and pertinent data are listed in Table 1. In addition to the stars listed there we measured one spectrogram each of the M 2.5 II–III star β Peg and the SRb variable L_2 Pup as a control on the accuracy of measurement and identification. Our measurements of those two stars are given in PWW. The uncertainties in wavelength due to blending are probably greater than the uncertainties of measurement.

For each plate, two independent analyses were applied to the measured and identified lines. First, a multiple linear regression analysis was used to look for correlations between the velocity and the excitation potential, ionization potential, line strength and wavelength of the line. Each of these possible dependences can be justified on physical grounds for an atmosphere with a velocity gradient; each has been individually noted as present on some plates.

More detailed information about the velocity structure of the atmosphere is obtained through a second analysis which was used for plates with well resolved lines. The histograms of the number of low and high excitation lines per velocity interval for these plates typically show well defined peaks, with one or more low excitation components and at least one high excitation component. Up to four distinct components can be identified on each plate, suggesting that the rising shock model with a single shock is too simple. Up to four velocity components with different excitation temperatures have also been found on infrared FTS spectra, e.g. for χ Cyg (Hall *et al.* 1979); for χ Cyg these components agree well with the histogram interpretation of the visual spectra (Wallerstein 1979; Willson 1979). This may be interpreted physically by assuming two shocks – an upper, low amplitude shock which dominates in the visible region and a lower, larger amplitude shock which dominates in the infrared. The average excitation potential for lines in each velocity bin was determined and found to be correlated with the peaks in the histograms, supporting the interpretation that the peaks are not due to selection effects in the line list but are the result of physical processes in the stellar atmosphere. The mean excitation potential for lines associated with a given peak can then be taken as an indication of strength (i.e. amplitude) of the corresponding shock.

Typically, the peak with larger displacement from the mean velocity has the higher mean excitation potential but fewer lines which is consistent with a larger amplitude, more energetic shock lying lower in the atmosphere. In the next two sections we will compare the velocity components as a function of time directly to the Hill & Willson (1979) formulation,

Table 1. Spectroscopic data.

Star	Days* from maximum	Date	Plate	Dispersion (Å mm^{-1})	Region	<1 eV	⩾1 eV	TiO	Emission	m_v* at max
RT Cyg	− 5	1975 September 22	DAO 10157	10	Y, R	15	26	39	1	6.8
	− 4	1975 September 23	DAO 10162	6	B	114	100		10	
	− 3	1978 April 30	DAO 12133			32	36			7.0
	+ 8	1977 April 30	Pb 14597	7	Y	8	19		1	7.5
	+ 8		Pb 14598	7	Y	8	19		1	
	+ 12	1956 July 14	Pc 2716	9	B	34	15	9	7	8.0
	+ 15	1974 September 24	DAO 9345	10	Y, R	7	37		1	6.7
	+ 16	1974 September 25	DAO 9351	10	Y, R	12	60		1	
	+ 25	1978 May 28	DAO 12199	10	Y, R	11	41			7.0
	+ 33	1972 September 13	DAO 7631	6	B	42	23			6.9
	+ 34	1972 September 14	DAO 7641	10	Y, R	16	62	46	1	
	+ 73	1972 October 23	Pd 13113	18	B					
Z Oph	− 17	1967 October 13	Pd 10318	18	B	15	9		4	8.0
	+ 12	1957 June 5	Pc 3184	13	Y, R	6	14		1	7.8
	+ 24	1957 June 17	Pc 3237	13	Y, R	7	35		1	7.8
	+ 24		Pc 3238	9	B	37	10		14	
	+ 36	1964 February 19	Ec 2688	16	Y	18	21		1	> 8.3
	+ 44	1964 February 27	Pc 7840	9	B	36	13		17	> 8.3
	+ 44		Pc 7846	13	Y, R	15	39		1	
S Car	− 9	1977 January 7	D895	9	B	75	56		2	6.2

* Dates and visual magnitudes at maximum from the AAVSO.
Plate designations are as follows: DAO = Dominion Astrophysical Observatory, 48-inch coude; Pb, Pc, Pd = Palomar Observatory, 200-inch coude; Ec = Lick Observatory, 120-inch coude; D = Cerro Tololo InterAmerican Observatory, 60-inch coude.

and find model parameters consistent with it on the assumption that we can see the effects of two shocks at the same time, i.e. that up to four velocity components are real.

3 The relationship between observed velocities and properties of the star

The process of interpreting the velocities of the absorption and emission lines in these stars involves three major steps:

(a) Distinguishing the lines which originate in different atmospheric regions and determining from these the apparent (heliocentric) pre-shock and post-shock velocities.

(b) Determining the shock parameters from the observed velocities:

(i) The difference, Δv_{obs}, between the observed pre-shock and post-shock velocities is multiplied by a geometrical correction factor p to obtain the shock amplitude, Δv.

(ii) A theoretical relationship for $\Delta v/v_0$ is then used to obtain the outward post-shock (v_0) and inward pre-shock ($\Delta v - v_0$) velocities relative to the star, and hence also v_*.

(c) Using the shock velocities to find physical parameters of the star.

The theoretical basis for the analytic model used in the interpretation of the present set of observations has been presented in Hill & Willson (1979). Since the model is needed in steps (b) and (c) above, we summarize key results of the theory here.

First, we need to relate position in the atmosphere to time. The ratio of the outward post-shock velocity, v_0, to the velocity of escape, v_e, was found by HW to remain nearly constant through the atmosphere. The ratio (called β) is typically 0.2 and cannot exceed 0.4 in a periodic solution. This very simple approximation to the results of numerical models allows the derivation of an analytic expression for the position of the shock front in the atmosphere at all times:

$$r_s(t) = r_s(0)\,[1 + c(t/P)]^{2/3}, \tag{1}$$

where P = period, t = time, r_s = shock position. For reasons discussed in HW the stellar radius is taken to be $r_s(0)$ and time zero is taken to occur at maximum visual light. The constant c depends on the mode of pulsation of the star and on the strength of the shock

$$c \simeq 28\,Q^d\,[\beta/0.2]\left[\frac{1+q}{1.2}\right], \tag{2}$$

where Q^d is the pulsation constant in days. It is approximately 3 for fundamental mode pulsation ($Q \simeq 0.1$ day) and 1 for first overtone pulsation ($Q \simeq 0.035$ day) (the quantity $q = (\Delta v/v_0)/(\rho_2/\rho_1 - 1)$ is small, $\simeq 0.1$). In accordance with the conclusions of Hill & Willson that the LPVs are predominantly pulsating in the fundamental mode, the analysis of the present material will emphasize the case $c = 3$; in the interest of completeness, however, we will include discussion of the differences expected if $c = 1$ instead.

3.1 THE GEOMETRICAL CORRECTION FACTOR

To derive the outward velocity of a layer of the atmosphere from the observed velocity we must first subtract the centre of mass velocity and then multiply by a geometrical correction factor p which takes into account the fact that we observe the line profile in light integrated over the disc. Parsons (1972) investigated the correction factor appropriate for use in Cepheids for Gaussian line profiles in a grid of plane parallel model atmospheres; he found that the most important effect on the correction factor comes from the finite width of the

line, with

$$p \approx 1.37 - 0.03\,(k/\Delta\lambda_{1/2})\,, \tag{3}$$

where k is the Doppler shift at the centre of the disc, $k \equiv \lambda_0(v/c)$, and $\Delta\lambda_{1/2}$ is the measured half-width at half-central depth. For the lines in the LPVs observed, as for the lines in the Cepheids studied by Parsons, $(k/\Delta\lambda_{1/2})$ generally is approximately 2, giving $p \approx 1.3$ for the plane parallel correction factor.

For the LPVs the plane parallel approximation only holds at maximum light; after that time the shock front moves to radii significantly greater than the stellar radius.

In order to take into account the changing geometry, let us re-examine the classical (delta-function line profile) derivation of the correction factor. The velocity observed will be the integral over the stellar disc

$$v_{\rm obs} = \int_{\mu_f}^{1} [v_r \mu]\, I(\mu)\mu d\mu \Big/ \int_{\mu_f}^{1} I(\mu)\mu d\mu\,, \tag{4}$$

where

$$\mu_f = [1 - (r_0/r)^2]^{1/2} \tag{5}$$

for a line formed at $r \geqslant r_0$, the stellar radius. For a limb darkening coefficient of 0.8 this gives

$$p_c(r) = \frac{(1-\mu_f^2) + 8(1-\mu_f^3)/3}{2(1-\mu_f^3)/3 + 2(1-\mu_f^4)}\,. \tag{6}$$

Parsons' results suggest that the limiting plane parallel correction factor should be reduced by 0.3 $(k/\Delta\lambda_{1/2})$ to $p_p(0) = 1.3$. In order to take into account, at least to first order, the finite-linewidth effect of Parsons we have chosen to multiply the classical result at $r > r_0$ by 1.3/1.375; the resulting factor, labelled $p_p(r)$ in Table 2, will be used to correct the data. When $(1.3/1.375)p_c(r) < 1, p_p(r) \equiv 1$ is used.

Using equations (1), (5) and (6) we have calculated correction factors as a function of time for $c = 3$ and $c = 1$; these values at representative phases are listed in Table 2. It is clear that for $c = 3$ (i.e. fundamental mode) geometrical correction effects become quite small beyond $t/P = 0.5$ and that the upper shock components $(t/P \geqslant 1)$ will not need any geometrical correction to the observed velocity. Since in the overtone model $(c = 1)$ the upper shock is at a smaller r/r_0, a small correction is still needed for the upper shock in that case.

Table 2. Geometrical correction factors.

	$c = 3$				$c = 1$			
t/P	r/r_0	μ_f	p_c	p_p	r/r_0	μ_f	p_c	p_p
0.00	1.00	0	1.375	1.31	1.00	0	1.375	1.31
0.05	1.10	0.412	1.292	1.23	1.03	0.251	1.345	1.28
0.10	1.19	0.543	1.234	1.18	1.07	0.345	1.317	1.25
0.15	1.28	0.625	1.194	1.14	1.10	0.412	1.292	1.23
0.20	1.37	0.682	1.165	1.11	1.13	0.465	1.270	1.21
0.30	1.53	0.758	1.125	1.07	1.191	0.543	1.234	1.18
0.50	1.84	0.840	1.082	1.03	1.310	0.646	1.183	1.13
0.70	2.13	0.882	1.060	1.01	1.424	0.712	1.149	1.095
1.00				1.0	1.587	0.777	1.115	1.06

Table 3. Approximate analytic solution parameters.

		[$Q_0 = 0.1$]	[$c = 3$]
Q	v_f/v_0	r/r_0	t/P
0.10	2.4	1.00	0.00
0.09	2.3	1.07	0.04
0.08	2.2	1.16	0.08
0.07	2.1	1.27	0.14
0.06	2.0	1.41	0.22
0.05	1.87	1.59	0.33
0.04	1.69	1.84	0.50
0.035	1.58	2.01	0.62
0.03	1.46	2.23	0.78
0.025	1.32	2.52	1.00
0.02	1.14	2.92	1.33
$\lesssim$0.015	1.0	3.54	1.89

3.2 INFALL VERSUS OUTFLOW

The ratio of the infall velocity ahead of the shock to the outflow behind the shock is also essentially purely a function of the mode (or more precisely of $Q(r) = PM^{1/2}r^{-3/2}$, where M and r are in solar units). An approximate intuitive derivation of v_f/v_0 was presented by HW; this piecewise continuous 'patch solution' gave values approximately 40 per cent larger than were found from the detailed hydrodynamic models. In Table 3 we therefore present v_f/v_0 versus Q derived from the 'patch solution' result divided by 1.40. In order to apply this to the observed velocity components as a function of time, however, we need to find $Q(r(t))$; in the second part of Table 3(a) the phase and (b) the location in the atmosphere corresponding to the values of Q tabulated are listed assuming for (a) $Q(r_0) = 0.1$ day (fundamental mode) and for (b) $c = 3$ (fundamental mode with $\beta = 0.2$).

3.3 IDENTIFYING THE ORIGIN OF SPECTRAL FEATURES

With the information contained in Table 3 we can determine the stellar centre of mass velocity from the simultaneous determination of the infall and outflow velocities around any single shock in the atmosphere. HW listed criteria for assigning spectral features to either the upper or lower shocks on the basis of the excitation and the behaviour with phase of the features. Guided by the results of the regression analysis, we can add to the HW list criteria for separating absorption features on a single plate according to the shock of origin:

(1) The wavelength interval of the plate will determine which shock is expected to dominate: for the relatively transparent Population II stars of the present study, blue plates (4000–5000 Å) show predominantly features originating in the upper shock, while red plates ($\gtrsim$ 7000 Å) show many lines from the lower shock. The opacity is expected to vary strongly with wavelength in this interval since the dominant source is presumably Rayleigh scattering.

(2) Lines originating in the lower shock will typically have higher excitation and ionization potentials than lines originating in the (smaller amplitude) upper shock.

(3) Lines from the lower shock are expected to be weaker, due to filling in of the continuum from overlying layers.

(4) The velocity amplitude (Δv) of the lower shock, even when reduced by a geometrical factor $\lesssim 1.3$, will be larger than the difference between components belonging to the upper shock (which do not need geometrical correction).

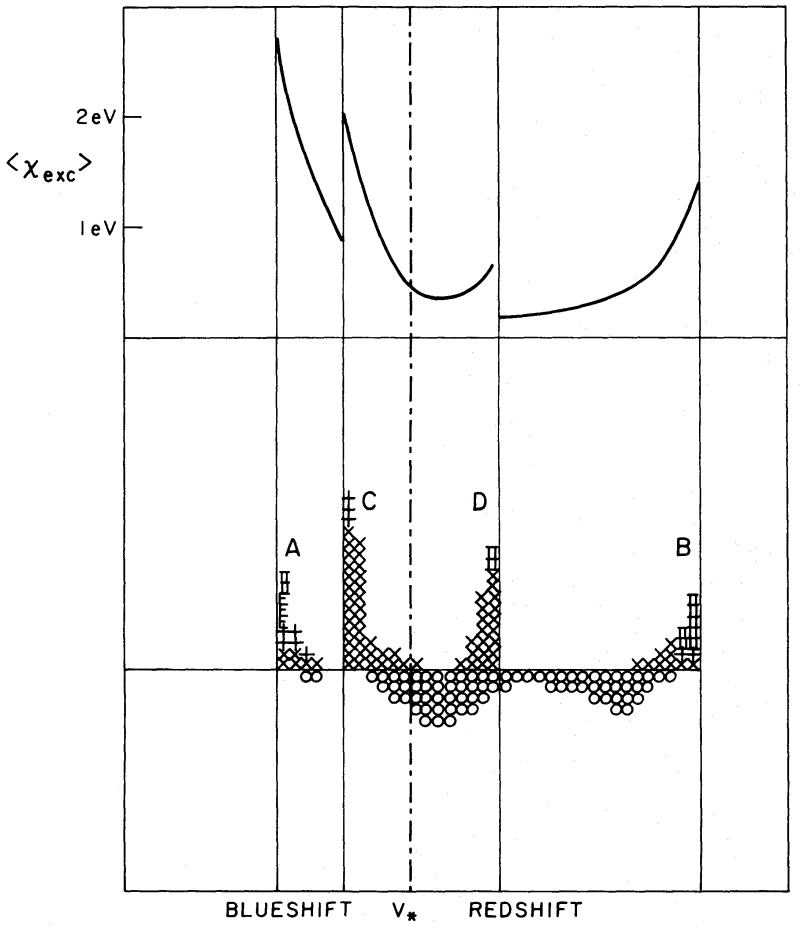

Figure 1. Hypothetical histogram for an ideal case near maximum light, showing the expected relative representation and excitation potential of lower shock (A, B) on upper shock (C, D) components. Here and in subsequent figures, (o) = low excitation lines (< 1 eV), (x) = moderate excitation (1–3 eV) and (+) = high excitation (> 3 eV) absorption lines; (II) are absorption lines from ions; (E) are emission lines from ions.

In the ideal case, then, we would expect to find high excitation, high Δv weak lines outlining the lower shock, and lower excitation stronger lines with velocities inside the range of lower shock velocities outlining the upper shock. This ideal situation is illustrated in Fig. 1. Further, one expects a comparison of red and blue plates taken at the same phase to verify the assignments made on other bases. In practice one can seldom (if ever) identify all four components on a single plate; further, the outward components of the upper and lower shocks do not differ much in velocity near maximum light after account has been taken of the geometrical correction factors. It is therefore nearly always necessary to compare a sequence of plates to determine the location and development of the features belonging to the two shocks and to determine the stellar velocity unambiguously.

3.4 THE USE OF SHOCK VELOCITY COMPONENTS TO DETERMINE STELLAR MASS AND RADIUS

The observed outward velocity behind the lower shock plus knowledge that $\beta \approx 0.2$ provides one constraint on the stellar mass and radius

$$\frac{GM}{r_0} = v_e^2 = \frac{v_0(0)^2}{\beta^2}. \tag{7}$$

The observed outward velocity behind the upper shock provides a second constraint:

$$v_0(P) = v_0(0)(1+c)^{-1/3}$$
$$= \beta(1+c)^{-1/3} v_e \,. \tag{8}$$

We can either assume we know c (i.e. assume both Q and β are known) and derive v_e again, hence (M/r_0), or use equation (22) of HW,

$$c \simeq \frac{3}{2}(1.2)\left(\frac{v_0(0)}{r_0}\right)P \tag{9}$$

and derive M versus r_0 for models of arbitrary Q consistent with the observed $v_0(P)$.

The infall velocities $v_f(0)$ and $v_f(P)$ do not provide independent constraints on M and r_0; their value lies in helping us establish the stellar velocity from the observed components, and/or determining the outward velocity (when it cannot be directly observed) from the stellar velocity and the infall velocity.

3.5 SUMMARY

In order to relate the components of the observed velocity distribution to the model velocity parameters we must first assign each component to one of the four possible layers: one above and one below each of the two shocks. We must then also determine the stellar velocity, and subtract that from each component. Then, the magnitudes of the velocities of the components must be multiplied by the appropriate geometrical correction factors. Finally, these velocities can be matched to a β=constant model to determine the mass and radius of the star.

4 Application to RT Cyg

RT Cyg has a period of 190 day, a relatively regular and symmetric light curve ($(M-m)/P = 0.44$) with a mean amplitude of 4.5 mag in the visual and $\gtrsim 0.88$ at 1.04 μm (Kukarkin *et al.* 1969; Lockwood 1972). Its velocity and period are consistent with its being a relatively old, low mass Mira of the same pulsation mode as the longer period ones (Feast 1962). Feast also notes that its luminosity class is Ib while for example the three Mira variables in 47 Tuc are luminosity class II-Ib.

4.1 THE REGRESSION ANALYSIS FOR RT CYG

The plates of RT Cyg are listed again in Table 4, where the phase (days from maximum), the wavelength region, the regression coefficients and the interpretation placed on these are given. Only significant and marginally significant coefficients (as defined by PWW) have been retained; significant coefficients are ones where the coefficient times the range of the variable on the plate exceeds the pre-fit standard deviation SD^0, and marginally significant ones fall between SD^0 and SD^f, the standard deviation after the fit.

Each set of coefficients has then been classified according to the four groups presented in PWW; the classification is summarized for reference in Table 5. In the last two columns of Table 4 we give the dominant component from the histograms (discussed in detail in the next section) and also a final interpretation of the regression results which takes into account all the 'corollary behaviour' of Table 5.

Table 4. Regression results for RT Cyg.

Plate	Days from max	Region	SD^o	SD^f/SD^o	$1/\lambda$	S	χ_i	χ_e	Case(s)	Interpretation	Dominant hi-ex. component on histogram
DAO 10157	− 5	Y	2.4	0.85	–	–	–	+ 2.5	a, c	Above shock	D (redder)
DAO 10162	− 4	B	2.0	0.89	+ 2.6	–	–	–	c, d	Shock in R.L.	D (redder)
YJ 12133	− 3	Y, R	3.88	0.95							
Pb 14597	+ 8	Y	6.6	0.88	–	–	+ 8.0	–	a, c	Large scatter suggests c: shock in R.L.	A and D blue and red
Pb 14598	+ 8	Y									
Pc 2716	+ 12	B	3.55	0.72	− 8.82	(+ 3.16)	(+ 3.36)	− 8.02	none	*Both* low and high exc. lines affected	0 volt
DAO 9345	+ 15	Y, R	4.6	0.59	+ 4.9	+ 10.7	− 4.7	–	d	Doubling of low exc. lines	A blue
DAO 9351	+ 16	Y, R			(+ 3.2)	–	− 6.4	–	(d)		A and C blue
YJ 12199	− 3										
DAO 7631	+ 33	B	2.0	0.88	− 2.9	–	–	–	a, b	Below shock	D and O
DAO 7641a	+ 34	Y, R	4.8	0.83	(+ 4.8)	+ 5.3	–	(− 4.5)	(d)	Doubling of low exc. lines	(A and C)
b			4.8	0.86	(= 4.1)	− 8.7	− 5.6	–	b	Below shock	(A and C) blue
Pd 13113	+ 73	B									

Table 5(a). Allowed coefficient signs.

X =	$1/\lambda$	S	χ_i	χ_e	Position of reversing layer relative to source of excitation	Velocity gradient (outward velocity positive)
Case						
a	–	–	+	+	above	positive
b	–	–	–	–	below	positive
c	+	+	+	+	below	negative
d	+	+	–	–	above	negative

Table 5(b). Shock model interpretation of regression coefficients.

Case	Region	Expected corollary behaviour
a	Above shock	Mostly low excitation lines ($\lesssim 1$ eV) Lines redshifted ($\lesssim 10$ km s^{-1}) Higher excitation lines more redshifted Small scatter in velocity
b	Below shock	Many higher excitation lines ($\gtrsim 1$ eV) Larger scatter than case a Lines at v_* to blueshifted ($\lesssim 5$ km s^{-1}) Higher excitation lines more blueshifted Dependence on ionization potential
c	c1. Immediate post-shock region	Very strong χ_i dependence Moderate scatter Blueshift predominant
	c2. Unresolved doubling and mixture of pre- and post-shock lines, especially high excitation lines	Very large scatter Two velocities – favoured in histograms Broad features and apparent blends at intermediate velocities Lines both redshifted and blueshifted compared to v_* Exclusion of high excitation lines should convert case c2 to case a, with lower scatter
d	d1. Immediate pre-shock region	Strong χ_e and χ_i dependence Small scatter
	d2. Unresolved doubling of low excitation lines	χ_e dependence Large scatter Broad features and apparent blends Exclusion of low excitation lines converts d to b, with smaller scatter

For the red and yellow plates there is a clear progression in the assignment of the region of origin of the lines with time. For the plates taken near maximum, the lines are formed predominantly above a shock, i.e. infalling, with some unresolved doubling presumably present particularly in the plates with large scatter. By +15 day the blueshifted components start to dominate on the red plates. For the first plates showing the effects of unresolved doubling it is the high excitation lines which are split; later the low excitation components show the effects of the shock. Hence we have, roughly, a progression from a to c to d as the shock rises through the atmosphere, affecting first the low lying higher excitation lines and later the lower excitation ones originating higher in the atmosphere.

Plate Pc2716 is particularly interesting since it shows two 'significant' coefficients and two marginally significant coefficients which together make up none of the four 'allowed' cases a–d. The two 'significant' coefficients alone would indicate case b, below the shock;

the marginally significant coefficients are consistent by themselves with case c, i.e. doubling of high excitation lines. The majority of the lines on this plate are low excitation, however, which coupled with the fact that the plate was taken in the blue wavelength region suggests that the lines on this plate are formed either between the two shocks or high in the atmosphere – in the region of HW's upper shock but not necessarily right at the shock, where the excitation would be higher. Hence the single shock cases do not apply.

The conclusion to be drawn from this analysis seems to be that the presence of at least one shock front in the reversing layer can explain the dependence of the velocity on the wavelength, line strength, ionization potential and excitation potential with complete consistency. Can an atmospheric velocity gradient, even one which evolves with time, equally well account for the dependences on wavelength, etc. found in Table 4? As discussed in PWW, case a corresponds to a positive outward velocity gradient with the excitation temperature increasing towards the star; case d may be interpreted as a negative outward velocity gradient with the excitation increasing inwards; cases b and c correspond to excitation temperature *increasing* with distance form the photosphere, and hence cannot correspond to a simple velocity gradient case. If we eliminate apparent cases b and c from Table 1 we find the progression a (red) and d (blue)→a (yellow)→d (red) and a (blue) with plate Pc2716 completely eliminated. The velocity field this would correspond to, assuming the red and yellow plates show lower regions of the atmosphere than the blue plates, is sketched in Fig. 2. On the basis of this picture one would expect a plate taken near +12 day in any wavelength interval to show very little scatter and no significant coefficients – instead, Pc2716 shows moderately large scatter and several significant coefficients. Also it is hard to imagine the 'travelling wave' of Fig. 2 not steepening into a shock as it travels throughout the atmosphere. Physically we expect a discontinuity; the simplest interpretation of the observed regression coefficients is that we have such a discontinuity passing through the line formation region as the cycle progresses.

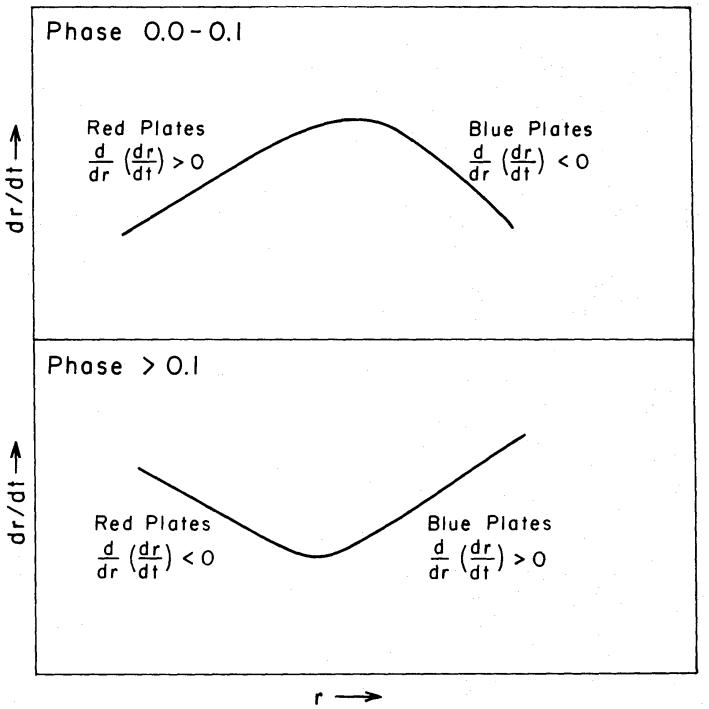

Figure 2. Velocity structure for RT Cyg on the assumption that no shocks are present, and only smooth velocity gradients occur.

4.2 HISTOGRAM ANALYSIS

The histogram analysis has several advantages over the regression analysis for the multiple component cases which are generally found: (a) it is quick and simple, (b) it is clear immediately which component most of the lines represent, and (c) it is possible to use the histogram analysis to distinguish lines formed in a given region – i.e. homogeneous groups of lines for use in e.g. abundance analyses.

The histograms for the RT Cyg plates are shown in Fig. 3(a)–(c). Where two plates were taken in the same wavelength region on the same night, where each plate has relatively few lines, and where the individual histograms were very similar we have combined two plates into a single histogram.

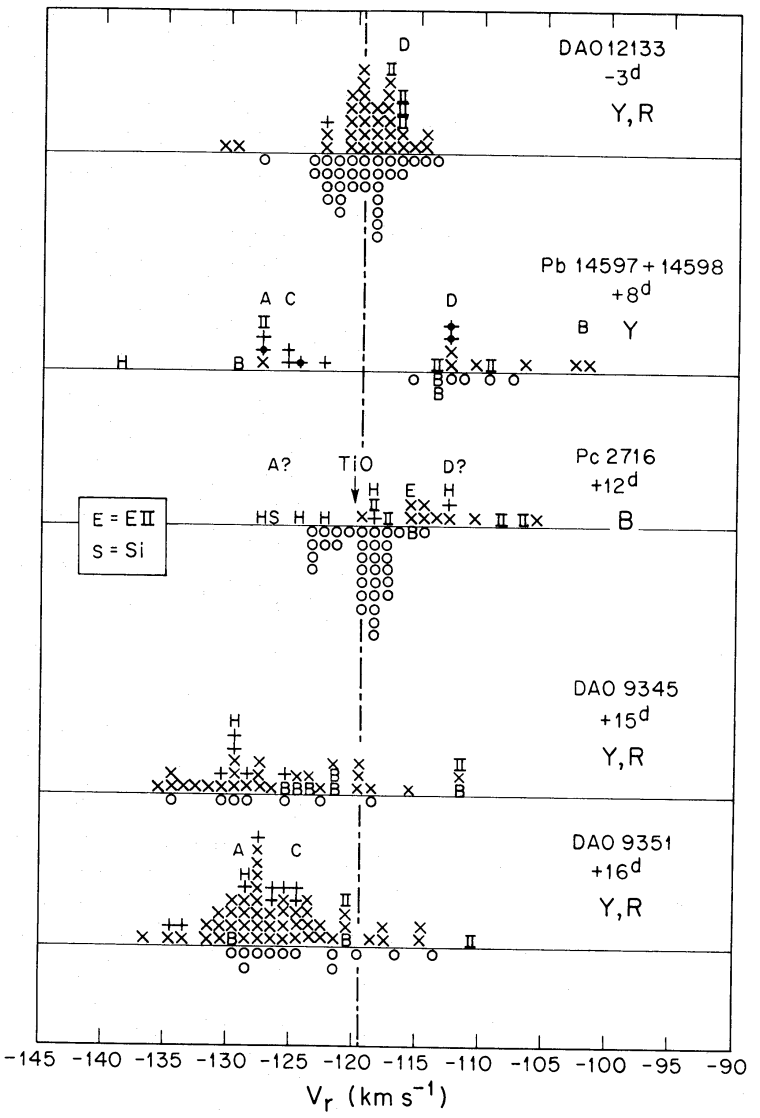

(a)

Figure 3. Velocity histograms for RT Cyg. Lines of 'high excitation' (arbitrarily chosen as $\chi_{ex} > 1$ eV) are plotted above the horizontal line; lines of low excitation (< 1 eV) are plotted below. Emission lines are indicated by the symbol for the element above the line; ion lines are shown as 'II' and emission from ions as 'EII'. Doubled lines are shown as a pair of dots at the appropriate velocities, above or below the line depending on their excitation class. A '+' sign indicates 'very high excitation' (≥ 3 eV) lines; where such lines are double the plus sign is superimposed on the large dot.

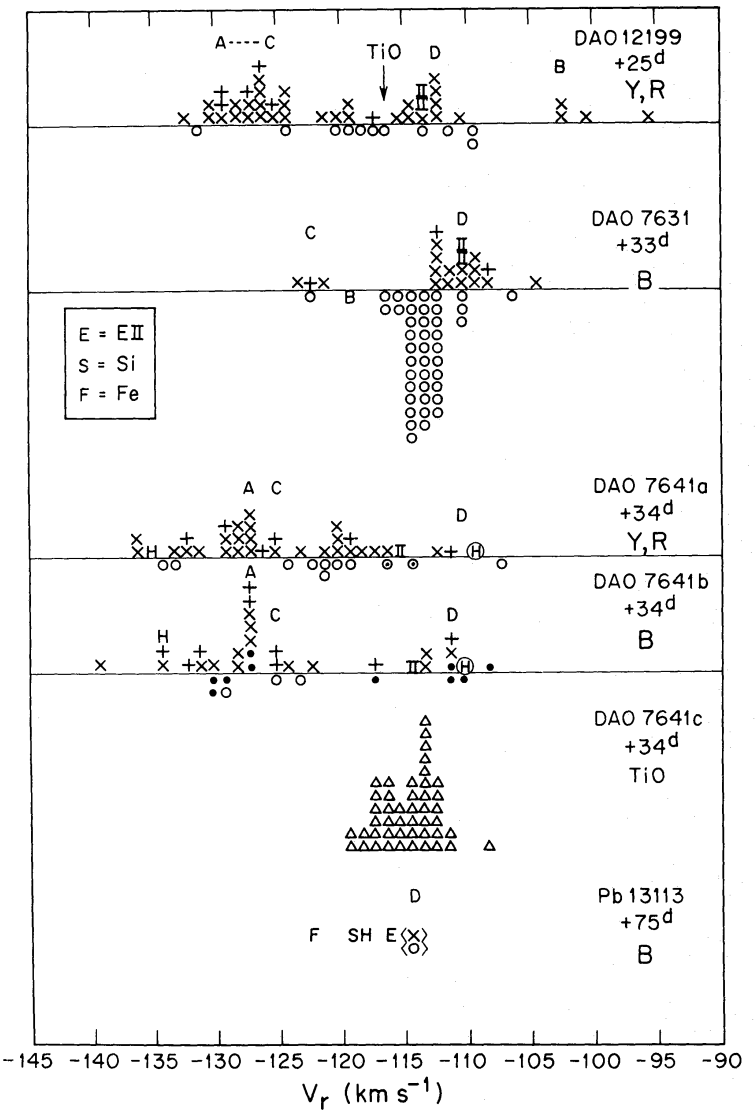

Figure 3 (b)

Before we can compare the velocities observed to the predictions of the model we must first (a) tentatively identify the region of origin of the lines producing a given peak on the histogram and (b) apply the appropriate geometrical correction factor $p(t)$. We have proceeded with the assignment of components as follows:

First, the blue plates were considered individually, and peaks marked. The heliocentric velocities of these peaks were listed and compared; recurrent features were found at -109 to $-110\,\mathrm{km\,s^{-1}}$ (high excitation), -112 and $-115\,\mathrm{km\,s^{-1}}$ (mixed high and low excitation), -122 to $-123\,\mathrm{km\,s^{-1}}$ (mixed), and a single plate showed also a low excitation component at $-118\,\mathrm{km\,s^{-1}}$. The red plates were then considered: persistent features appeared there at -127 (to -135?)$\,\mathrm{km\,s^{-1}}$ (high excitation), -110 to $-112\,\mathrm{km\,s^{-1}}$ (high excitation), $-115\,\mathrm{km\,s^{-1}}$ (on one plate) and $-102\,\mathrm{km\,s^{-1}}$ (high excitation lines of low to moderate strength – two plates but not very many lines). We then tentatively identified the (blue plate) components at -110 ± 2 (seen also weakly on the red plates) and -122 to $-123\,\mathrm{km\,s^{-1}}$ (also seen on a few red plates) as corresponding to the upper shock velocities of outflow and infall. Using Table 3 for v_f/v_0 at $t = P$ we derive a stellar velocity around $-117\,\mathrm{km\,s^{-1}}$ but with considerable uncertainty due to the tendency of upper shock lines to shift from cycle

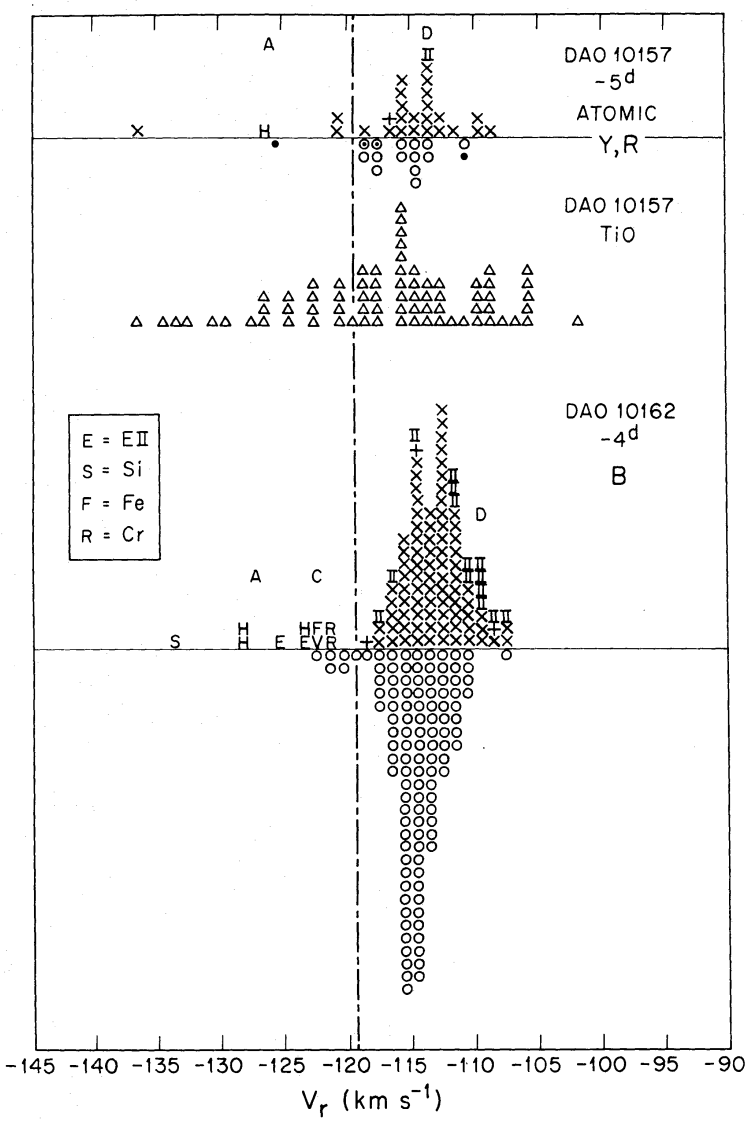

Figure 3(c)

to cycle (HW). The components at -102 and $-127\,\mathrm{km\,s^{-1}}$ then are assigned to the lower shock; again applying v_f/v_0 from Table 3 gives a stellar velocity of $-119\,\mathrm{km\,s^{-1}}$. Note that no geometrical correction is necessary here, since the ratio v_f/v_0 determines v_*. The remaining components from -113 to $-118\,\mathrm{km\,s^{-1}}$ consist primarily of low-excitation lines and TiO. These we assume to be blends and/or components formed either between shocks or far enough out to have velocities roughly equal to the stellar centre of mass velocity. The assignment of components outlined above is diagrammed in Fig. 4.

After this tentative assignment of components was made we returned to the histograms and marked each with its most probable region of origin: A = post-shock, lower shock; B = pre-shock, lower shock; C = post-shock, upper shock and D = pre-shock, upper shock. These assignments are shown in Fig. 3. Note that it is often difficult to separate the post-shock components from the upper and lower shocks, since $[v_0(0)/p_p(0)]/v_0(P) \approx 1.2$; thus with $v_0(0) \simeq 10\,\mathrm{km\,s^{-1}}$ the separation of these two components is typically less than $2\,\mathrm{km\,s^{-1}}$ which is of the order of the scatter found on plates of this resolution for β Peg (PWW). Thus the exact position and assignment of components A and C are less certain than are the assignments of B and D, where the progression in the ratio v_f/v_0 with time outweighs the

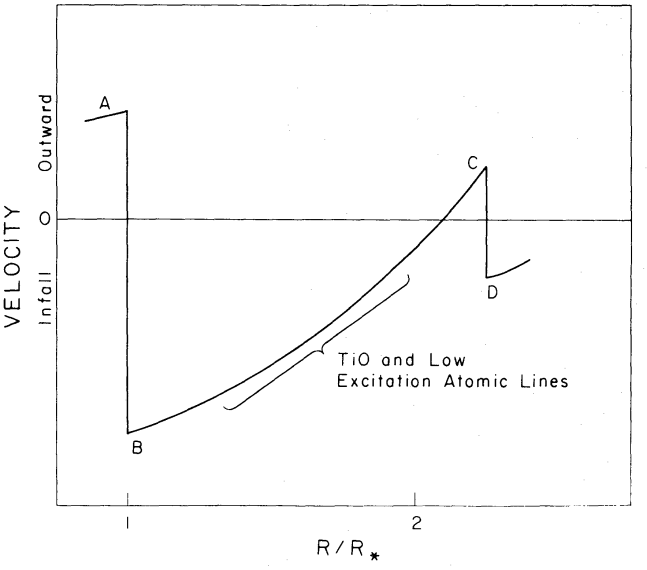

Figure 4. Assumed velocity structure for RT Cyg near maximum light, and the origin of major features in the histograms.

effects of p_p. Unfortunately lines formed at B tend to be relatively weak, due to the filling in of the continuum by higher atmospheric layers, and not many have been measured on these plates.

Once each individual feature has been assigned to a region of formation and a stellar velocity has been selected we can find the velocity of each region with respect to the star, using the factor p_p from Table 2 appropriate for each region at the observed phase to correct

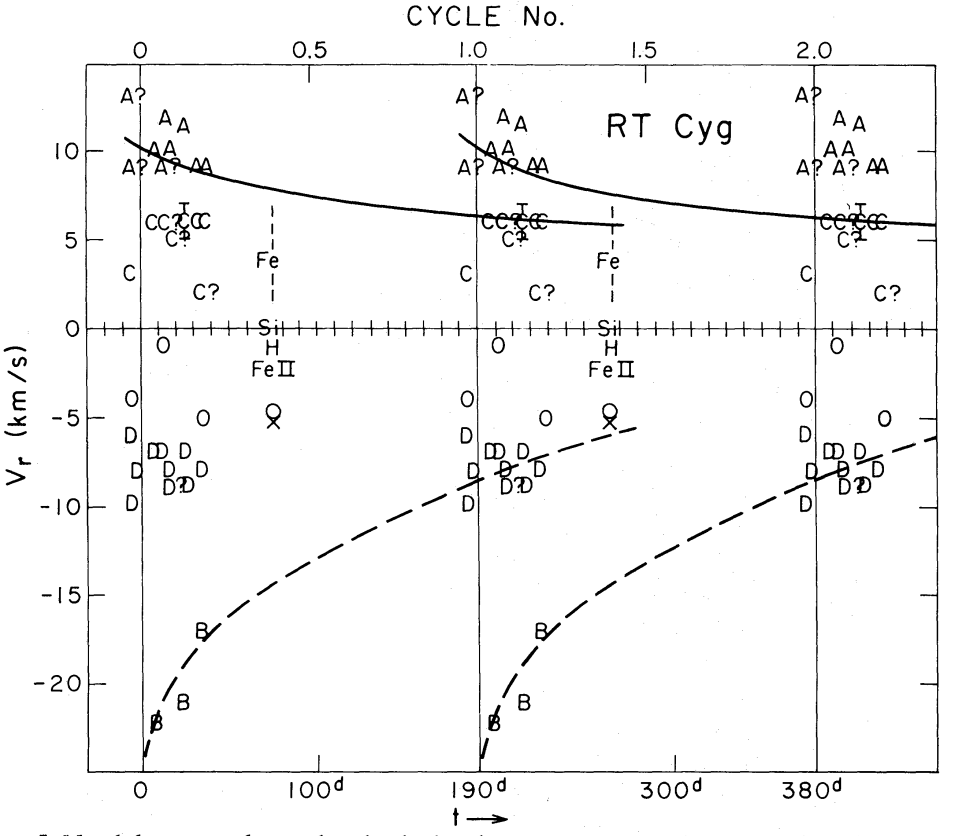

Figure 5. Match between observed and calculated components of velocity as a function of phase.

the observed displacement. The results of this procedure, with $v_* = -119\,\mathrm{km\,s^{-1}}$, are displayed in Fig. 5. The low excitation components (O) and the location of the TiO features (with no geometrical correction factor applied) are also indicated in Fig. 5. Note that the ion lines (II on Fig. 3a and b) tend to be formed just ahead of the shock front(s) – presumably due to radiative pre-ionization – thus the component D is taken at the velocity of the ion lines rather than the peak in the excited lines in plates DAO 10162, 12133 and 12199.

4.3 EMISSION AND ABSORPTION LINES AT +75 DAY

One plate, Pd13113, taken at +75 day was available for inclusion in this analysis. Since the resolution is not as high as for the other plates, only mean velocities are indicated for the emission lines and for the low and high excitation absorption lines.

The observed features are also shown in Fig. 5 with no correction factor applied. The absorption lines are apparently being formed above the upper shock, and fit well on the 'D' portion of the line; the Fe I emission appears to be originating from the region behind the upper shock while Si and H emission appear near the stellar velocity. As was argued by Willson (1976) if the H and Si lines are formed in an optically thin shell at r_s, the apparent shift will be

$$\delta v \simeq \frac{1}{2} v_0 \{1 - [1 - (r_0/r_s)^2]^{1/2}\} . \tag{10}$$

If we assume the 'shell' is the region immediately behind the lower shock, then at +75 day

$$\frac{r_s}{r_0} = \left[1 + c\left(\frac{75}{190}\right)\right]^{2/3} = \begin{cases} 1.68 & c = 3 \\ 1.25 & c = 1 \end{cases} \tag{11}$$

and hence the observed velocity is expected to be

$$v_{\mathrm{obs}} = \begin{cases} 0.1\, v_0 & \text{if} \quad c = 3 \\ 0.2\, v_0 & \text{if} \quad c = 1 . \end{cases} \tag{12}$$

At phase +75 day, $v_0 \simeq 8\,\mathrm{km\,s^{-1}}$ ($c = 3$) (or $\sim 6\,\mathrm{km\,s^{-1}}$ if $c = 1$) so we would expect to observe a line shift $\lesssim 1\,\mathrm{km\,s^{-1}}$ ($c = 3$) (or $\lesssim 1.2$ if $c = 1$). The observation that the Si and H emission lines fall at the stellar velocity (within the observational probable error of $\pm 2\,\mathrm{km\,s^{-1}}$) at this phase is entirely consistent with the hydrogen lines being formed behind the lower rising shock, which has become optically thin and has reached a radius substantially larger then the photospheric radius at this phase.

4.4 THE REGION OF ORIGIN OF THE TITANIUM OXIDE BANDS

The average velocity of the TiO lines as measured for DAO 10157, DAO 12199, Pc2716 and DAO 7641 are indicated by the arrows on the histograms. In general, the TiO components are very similar to the low excitation atomic lines in that they show moderate to large scatter around an average velocity close to the stellar velocity. As we did for the low excitation lines, we attribute this behaviour of TiO to its origin either between our two principal shocks or above the upper shock.

4.5 COMPARISON WITH THE HILL–WILLSON MODEL

The solid line in Fig. 5 is determined by equation (1) for $c = 3$ using $v_0 \simeq v_s/(1 + q)$, where $(1 + q) \approx$ const, with $v_0(0)$ taken as $10\,\mathrm{km\,s^{-1}}$ from the mean of the observed A component

velocities. It passes close to the C components; if we did not have the problem of confusion of A and C components discussed earlier we would be likely to have a few C components at higher v_r, and that would improve the fit. We therefore take the correspondence between the line and the location of the C components to indicate a consistent fit. From the solid line and Table 3, assuming $Q(r_0) = 0.1$ day, we can derive $v_f(t)$; this is plotted in Fig. 5 as a dashed line. It clearly fits both the B and D components quite well. We have forced the B component fit through our use of the A and B components to find v_*, but the fit to the D components (as to the C components above) are governed only by our choice of $v_0(0)$ plus the model ($\beta = 0.2$, $Q_0 = 0.1$). We also have not forced the fit to the variation of the B components with time.

Conclusion: we have identified four shock velocity components in these plates of RT Cyg; these components are consistent both qualitatively and quantitatively with the model presented in HW for $c = 3, \beta = 0.2, Q_0 = 0.1$ day.

4.5.1 Derivation of physical parameters for RT Cyg from the four component interpretation

Taking $10\,\mathrm{km\,s^{-1}} = v_0(0) = \beta v_e(0)$ produces a relationship between M and R shown on Fig. 6 for $v_0(0) = 10 \pm 1\,\mathrm{km\,s^{-1}}$. The components C and D also provide a constraint on M and R as discussed in Section 2; this curve is also shown in Fig. 6 for $v_0(P) = 6 \pm 1\,\mathrm{km\,s^{-1}}$. These two lines intersect near $M = 1\,M_\odot$ and $R = 10^{13}$ cm. On Fig. 6 we have also plotted the mass–radius relation from theoretical Q values for fundamental mode and overtone pulsation for $P \approx 190$ day from Wood (1975). The line for fundamental mode pulsation ($Q = 0.1$ day) passes very near the intersection of the $v_0(0)$ and $v_0(P)$ lines. From the confluence of these three lines we find the probable mass and radius of RT Cyg:

$$M \simeq 0.7\text{–}1.0 M_\odot; \quad R \simeq (1.0 \pm 0.2) 10^{13}\,\mathrm{cm}.$$

Note that the mass derived from the velocity analysis is completely consistent with RT Cyg being a member of the old disc population, as its large space velocity and short period have already indicated it must be.

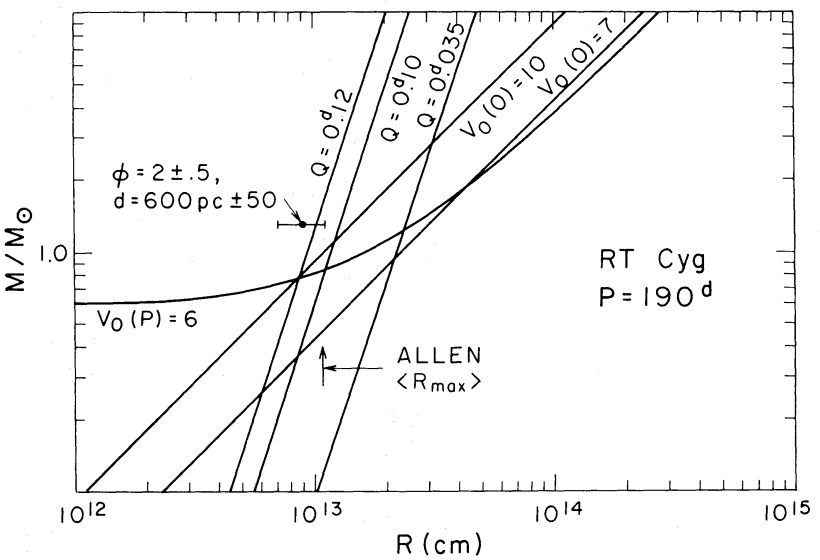

Figure 6. Mass–radius plot for RT Cyg, showing confluence of $\theta \sim 0.1$ day, $v_0(P) \approx 6$, $v_0(0) = 10\,\mathrm{km\,s^{-1}}$ lines near $M \sim 0.9 M_\odot$, $R \sim 10^{13}$ cm.

4.5.2 Is there an alternative interpretation involving only two velocity components?

Although the blue and red plates seem to indicate four different velocity components, which can be interpreted to give a consistent and reasonable physical model, we should consider whether an equally consistent and reasonable model could be derived from a simpler interpretation of the observations. We have already mentioned that the A and C components are difficult to separate from each other, and that very few lines are available to give us the B component. If we ignore the B component lines, using the D component for the infall velocity, and combine the A and C lines into a single determination (with large uncertainty), then we need only invoke a single shock to interpret the histograms. Presumably, the only shock would then be the lower or 'photospheric' shock in the HW model. Since we have deleted the relatively high velocity B component, the shock we have here has a (geometrically corrected) amplitude of only $\sim 19\,\mathrm{km\,s^{-1}}$.

A shock with an amplitude of $19\,\mathrm{km\,s^{-1}}$ at photospheric densities is not likely to ionize sufficient hydrogen to produce the strong observed emission lines; $\Delta v \gtrsim 25\,\mathrm{km\,s^{-1}}$ is required (Gorbatskii 1961; Tsuji 1971). So low an amplitude occurs with $Q = 0.1$ day only if the mass is implausibly low – less than $0.3\,M_\odot$ – so we will consider in this case only overtone pulsation, with $Q = 0.035$ day. Using v_f/v_0 for $Q = 0.035$ day then gives $v_0(0) = 7\,\mathrm{km\,s^{-1}}$; this line for $\beta = 0.2$ has also been drawn in Fig. 6. The stellar velocity derived using $v_f/v_0 \simeq 1.6$ for $Q = 0.035$ day and the (A + C) D components is $\approx -123\,\mathrm{km\,s^{-1}}$ rather than $-119\,\mathrm{km\,s^{-1}}$ in the two-shock case. Since we are now dealing with only one shock, we have no second velocity constraint on the mass and radius. However, the lines for $Q \simeq 0.035$ day and $v_0(0) = 7\,\mathrm{km\,s^{-1}}$ intersect at a reasonable mass – $M \simeq 0.95\,M_\odot$. It is thus possible to make an internally consistent one-shock overtone pulsation model from the observed velocities as well as the previously discussed two-shock, fundamental mode model. We need to look for independent (external) constraints to distinguish between the possible models.

Two such constraints are available. First, in the preceding section we applied the same analysis to RT Cyg which has previously been applied to χ Cyg, R Leo and o Cet (HW; Willson 1979; Wallerstein 1979); stars which have up to four components well established from infrared measurements. Here we have derived compatible R, M, and mode of pulsations for RT Cyg assuming four components; we find it pulsating in the same mode as the longer period stars. If the two component model applies to RT Cyg, however, that means it is pulsating in a different mode from these longer period stars, and that is not consistent with its relation to them in P, M, population, etc.

The second constraint is the observed size of the star. Pettit & Nicholson (1933) observed RT Cyg three times using water cell absorption to obtain red magnitudes. Using the recalibration of their water cell magnitudes by Payne-Gaposchkin & Whitney (1976) we derive the angular diameter at three phases shown in Fig. 7. More recently, Barnes & Evans (1976; see also Barnes, Evans & Moffet 1978) have combined $(V-R)_J$ measurements with angular diameters determined near 7000 Å to calibrate a relationship between surface brightness F_V and colour $(V-R)$ which can then be used to determine the angular diameter of any other star for which $(V-R)_J$ is measured. Since their 'observed' F_V versus $V-R$ relationship is heavily influenced beyond $V-R \simeq 2$ by a single R Leo angular diameter measurement which does not correspond to an observed colour, and this relationship gives unphysically large angular diameter variations, we shall use here a modified surface brightness relation defined very simply from the o Cet points listed by Barnes & Evans by (a) the original fit up to $V-R = 2.3$ and (b) the line connecting two o Cet points (without limb darkening) beyond $V-R = 2.3$. Combining this version of F_V versus $V-R$ with the observations of RT Cyg from Barnes (1973) gives the points marked '+' in Fig. 7. Note that reddening has small effect on the derived ϕ since the changes in V and $V-R$ nearly cancel.

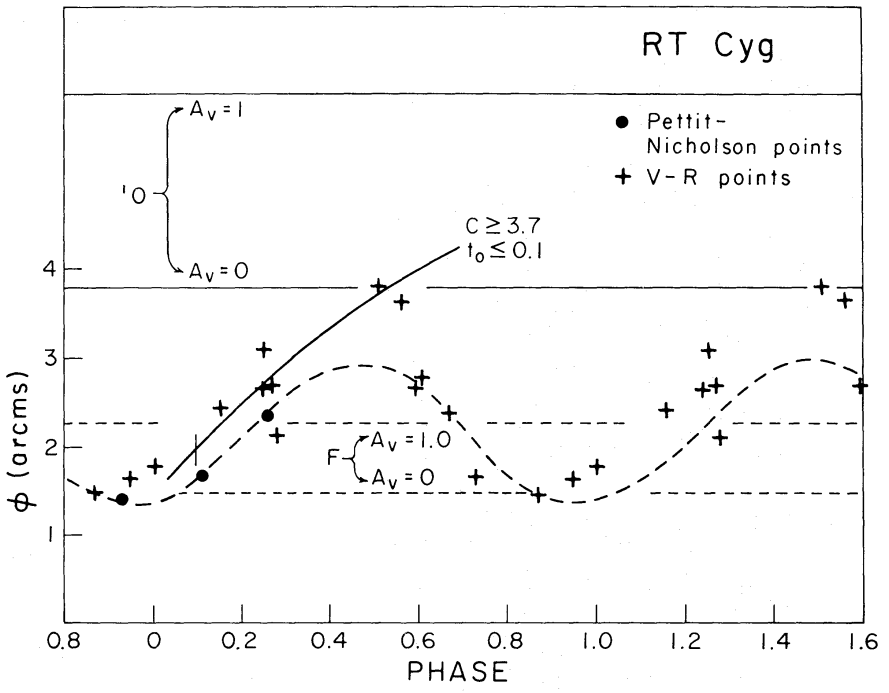

Figure 7. Variation of the angular diameter of RT Cyg with phase from: (+) F_v versus $V-R$ as described in the text), (•) Payne-Gaposchkin & Whitney's (1976) recalibration of Pettit & Nicholson's (1933) measurements compared with the expected fundamental mode (F) and Overtone mode (^{1}O) angular diameters assuming $M \approx 1\,M_\odot$ and distances from Feast's Mv, observed v assuming interstellar absorption $A_v = 0, 1$ as indicated.

Near maximum the $(V-R)_J$ and water cell determinations agree very well. The 'discontinuity' in the angular diameter as a function of time from $V-R_J$ suggests that the visual surface brightness is dominated by the rising shock front during the early part of the cycle. The solid line in the figure indicates $r_s(t)$ for $c = 3.8$, if $r_0 = r_s$ at phase $t_0/P = 0.1$ in equation (1). (Note that the derived c is very sensitive to the choice of t_0/P; decreasing t_0/P increases c.) The sine curve has been sketched in to indicate a possible 'photospheric' variation over the cycle consistent with the three points observed by Pettit & Nicholson.

According to Clayton & Feast (1969) the absolute visual magnitude of a 190-day Mira variable is about -2.4 (interpolating between two groups). The observed mean apparent magnitude at maximum light of RT Cyg is $+7.3$, implying a distance of $\lesssim 870$ pc for RT Cyg (less if there is significant interstellar absorption in the direction of RT Cyg★). Dividing the fundamental mode value for the diameter and the overtone mode value for the diameter (for $M \leqslant 1\,M_\odot$) each by this distance produces the angular diameters marked F and ^{1}O on Fig. 7. Although it is not obvious from the plot what is the best radius for RT Cyg, the F mode values appear significantly more consistent with the observed angular diameters than the ^{1}O mode values. Further, the addition of appreciable reddening to the star will improve the F agreement and lessen the agreement with the ^{1}O value.

4.6 SUMMARY

We conclude therefore that although it is possible to interpret the velocity observations of RT Cyg in terms of either a fundamental mode, two-shock model or an overtone mode, one-

★ Interstellar D lines are present but weak. At its galactic latitude of 12° interstellar absorption should not be large.

shock model, both the observed angular diameter and the consistency of the model with that successfully used for the longer period stars previously analysed favour the two-shock, fundamental mode pulsation interpretation for RT Cyg. Ultimately a direct measure of either the lower shock amplitude (near 2 μm) or the stellar centre of mass velocity (e.g. microwave thermal or maser lines) should be able to remove this ambiguity.

5 S Car

S Car has a period of 149.5 day; the light curve is very symmetric ($(M-m)/P = 0.51$) with a mean amplitude of 2.8 mag in the visual (Kukarkin *et al.* 1976). The spectral type near maximum is K5e (Keenan 1966). A very extensive analysis of the spectroscopic variations in S Car over several cycles is given in Shinkawa (1973); we will make extensive use of her results in interpreting our single blue spectrogram, D895, taken 9 days before maximum in 1977.

5.1 THE DEPENDENCE OF VELOCITY ON EXCITATION AND IONIZATION POTENTIAL

The regression analysis for D895 gave significant dependence on ionization and excitation potential (PWW), both positive. This is consistent with case a (lines formed above the source of excitation, velocity gradient positive) or case c (lines formed across shock; high excitation lines are doubled). Shinkawa investigated the dependence of the velocity on excitation potential around the cycle; she found positive coefficients near maximum light and negative ones near minimum light. This is very similar to our results for RT Cyg, and implies the same progression from (a, c) to (d, b) we found for that star. That is, the dependence of the velocities on excitation potential can be accounted for by a shock rising through the region of line formation as the cycle progresses.

5.2 VELOCITY COMPONENTS

The histogram of velocities for our plate of S Car is shown in Fig. 8; the peaks marked on Fig. 8 are reproduced in Fig. 9, which shows Shinkawa's velocities as a function of phase from her 'red' and 'infrared' plates.

From phase -0.02 to phase $+0.9$ we can fit the infrared plate velocities with a linear dependence on phase: $v = 276.9 + 22.6\ (t/P)\,\mathrm{km\,s^{-1}}$ (coefficient of determination $r^2 = 0.85$), which extrapolates to $v = 299.6\,\mathrm{km\,s^{-1}}$ at phase 1.0. On the histogram we note a cluster of ion lines around $300\,\mathrm{km\,s^{-1}}$; this group of lines must then be formed in the region immediately ahead of (above) the lower shock, and hence component B here falls at $v = 300\,\mathrm{km\,s^{-1}}$, and A at $276.9\,\mathrm{km\,s^{-1}}$. At -9 days from maximum our blue plate clearly does not show any lines from the material rising behind the lower shock; that is, component A is not seen in the histogram. The two major peaks in the histogram, at $+280$ and $293\,\mathrm{km\,s^{-1}}$, we assign to the upper shock components C and D, leaving an apparent 'extra feature' at $296\,\mathrm{km\,s^{-1}}$ to be accounted for. Note, however, that the region ahead of the lower shock, component B, appears to contain primarily ions (Fe II, Ti II, etc. presumably ionized by radiation from the shock). Thus few neutral atomic lines of those elements which normally produce the visible absorption lines can come from this region. There must be a minimum distance ahead of the shock where these elements can remain neutral; near this boundary the density (increasing inwards) is highest giving the 'extra' peak.

The velocity structure of S Car's atmosphere at maximum deduced above is shown schematically in Fig. 10(a).

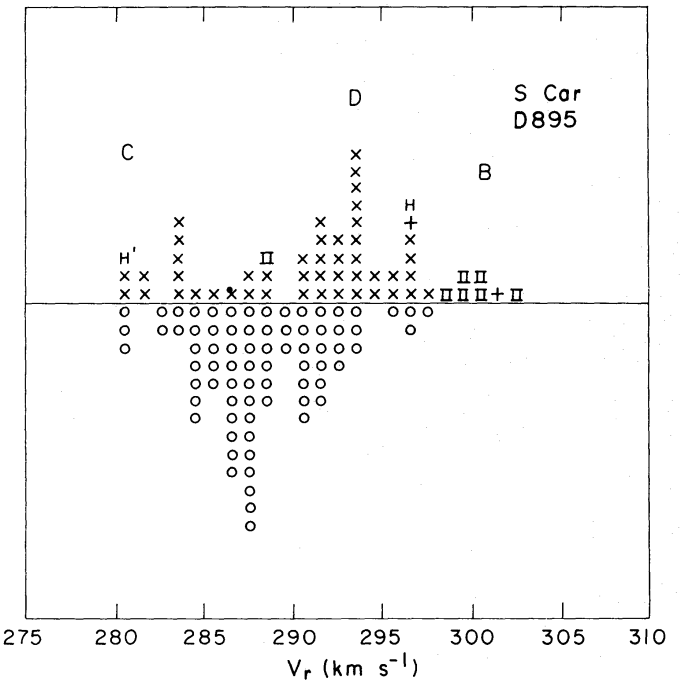

Figure 8. Histogram for S Car plate D895 taken 9 days before maximum in 1977. Components are labelled as in Fig. 3.

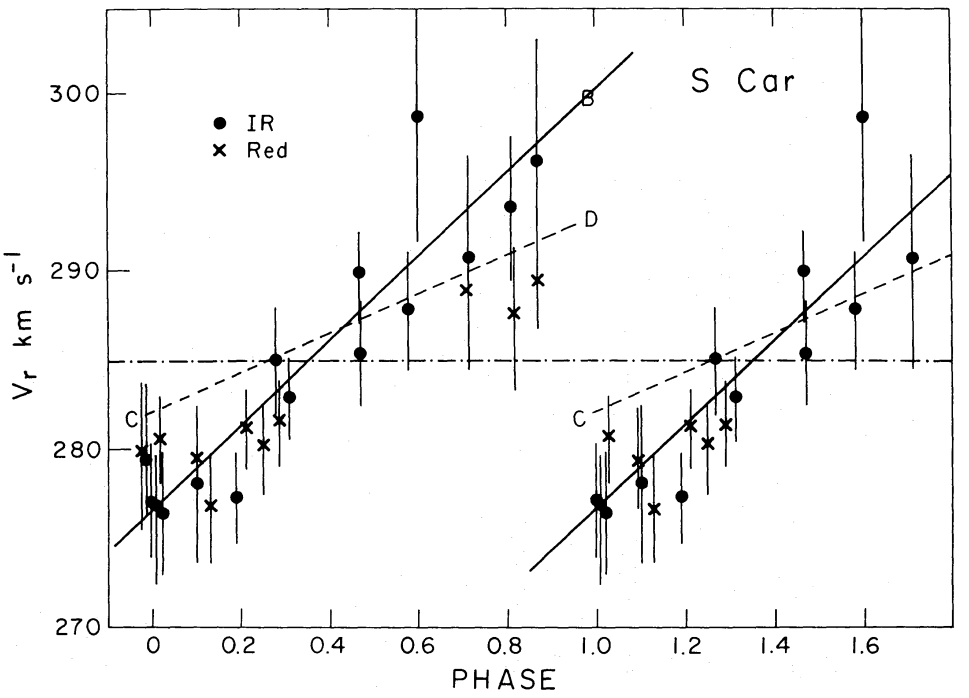

Figure 9. Comparison of component velocities from D895 with Shinkawa's (1972) velocity versus phase for S Car. The solid line is the regression fit for Shinkawa's 'IR' velocities (ϕ); the dashed line joins our components C and D. The letters B, C, D give the velocities from the histogram for RT Cyg, Fig. 8. The (*) mark Shinkawa's 'red' velocity components; the dot-dash line is our derived v_*.

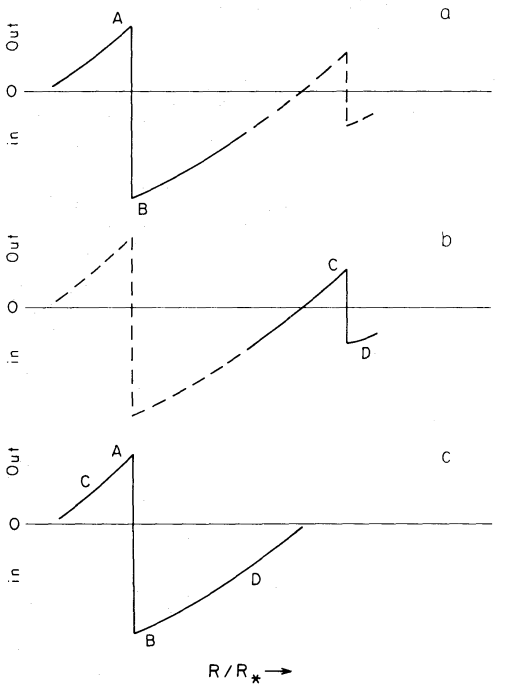

Figure 10. Velocity structures for S Car as a function of phase: (a) velocity structure near maximum showing the origin of the infrared components in the lower shock, with the upper shock indicated by dashed lines; (b) the origin of the red components in the two shock model; (c) the origin of the red components if only one shock is assumed.

5.3 PHYSICAL INTERPRETATION OF THE COMPONENT VELOCITIES

From the observed or derived components A and B we can deduce the stellar velocity and the parameters of the lower shock near maximum light:

$$\Delta v(0) = P\Delta v_{\rm obs}(0) = 23 \times 1.3 = 30\,{\rm km\,s^{-1}},$$

$$v_0(0) = \frac{\Delta v(0)}{1 + v_0/f_{\rm f}} = 30/3.4 = 9\,{\rm km\,s^{-1}},$$

$$v_* = 23/3.4 + 277 = 284\,{\rm km\,s^{-1}}.$$

Similarly for the upper shock

$$\Delta v(P) = 13\,{\rm km\,s^{-1}}, \qquad v_0(P) = 13/2.3 = 5.6\,{\rm km\,s^{-1}}, \qquad v_* = 286\,{\rm km\,s^{-1}}.$$

The small difference in the stellar velocity from the upper and lower shock components is only marginally significant; it may also be explained by reference to the behaviour of the numerical models. As was discussed by HW, aperiodicities (cycle to cycle differences) are frequently found in the upper shock components. Often, in the models, the aperiodicity preserves the shock amplitude while shifting the velocity components one way or the other. Therefore we have chosen to set the stellar velocity for S Car using the lower shock components, and to use the upper shock amplitude from this one plate to determine $v_0(P)$ directly without regard to the apparent difference in v_* implied by this approach.

The mass–radius plot for S Car is given in Fig. 11. The lines for $v_0(0) = 9\,{\rm km\,s^{-1}}$ and $Q = 0.1$ day intersect near $M = 0.6M_\odot$, $R = 0.85 \times 10^{13}$ cm. This may be compared with values obtained recently by Robertson & Feast (1981) from *JHKL* photometry: from their

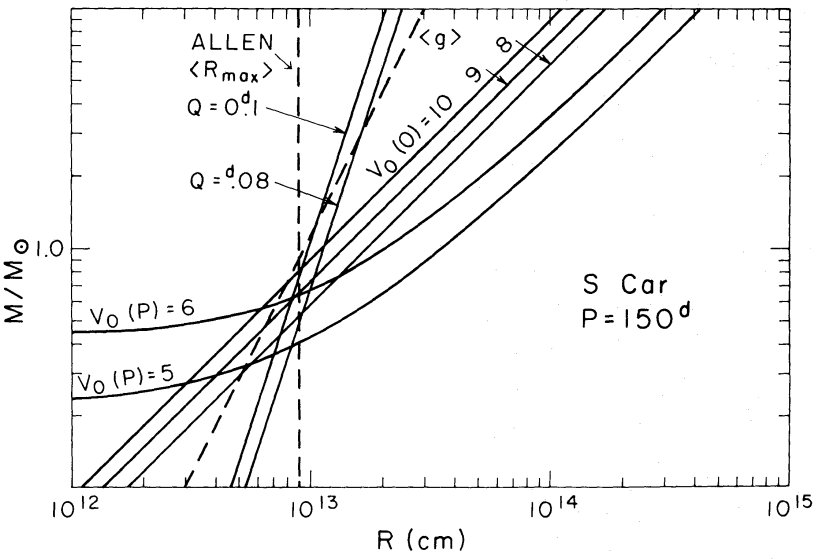

Figure 11. Mass versus radius for S Car – constraints from pulsation theory ($Q \sim 0.1$ day) and observed velocities are shown.

Table 3 the radii of $\langle P \rangle = 375$ day Miras are 2.7×10^{13} cm, of $\langle P \rangle = 225$ day Miras are 1.6×10^{13} cm, and of the anomalous 123 day 'Miras', 4.9×10^{12} cm. A linear fit to $\log R$ versus $\log P$ using all three groups implies $R = 7 \times 10^{12}$ for $P = 150$ day; extrapolation from the longer period groups (excluding the anomalous 123 day stars) gives $R(150\text{ day}) = 1 \times 10^{13}$ cm. These values effectively bracket the value obtained from the velocity analysis.

A further constraint on the mass and radius of S Car may be obtained from estimates of the surface gravity. Shinkawa has determined the surface gravity for S Car by comparing model atmosphere calculations with the observed flux distribution; she finds a mean value of $\log g = +0.1$, but with a variation over the cycle from $\log g = -0.9$ to $+1.1$. She also notes that the maximum acceleration derived from velocity variations of the lines is 1 cm s^{-2} or $\log g = 0.0$. The locus of $\log g = 0.0$ is shown in Fig. 11; it falls slightly above the point (M, R) selected from the shock components, but is not significantly different considering the uncertainties in g. Or, conversely, $M = 0.6 M_\odot$ and $R = 0.85 \times 10^{13}$ cm give $g = 1.85$ cm s^{-2}, which agrees well with both the value obtained from the observed flux distributions and the maximum observed acceleration.

A comment on the evolutionary significance of the observed mass: since stars with $0.6 M_\odot$ initially are not expected to have evolved off the main sequence yet, such a low mass may indicate that significant mass loss has already occurred from S Car – perhaps up to 30 per cent of its initial mass. Shinkawa found that the elements barium, lanthanum and europium are overabundant relative to iron in S Car; although this conclusion may not be confirmed when studies are made which take departures from both plane parallel geometry and from hydrostatic equilibrium into account, it does suggest the possibility of finding anomalous abundances for this star due to nucleosynthesis, mixing and mass loss.

5.4 VELOCITY GRADIENTS OR MULTIPLE SHOCKS?

We have shown that the observed velocities are consistent with a two-shock interpretation. As with RT Cyg we ask: are the Shinkawa results and our results consistent with any other picture, such as a single shock and velocity gradients? The regression fit for S Car shows significant positive dependence on χ_i and χ_e, meaning the lines are either formed above a

shock (case a) or across a shock (case c) with the higher excitation lines split. Hence they suggest a shock in the lower portion of the reversing layer near maximum light. The velocity structure which must therefore obtain near maximum light to explain both Shinkawa's IR plates and our regression analysis is shown in Fig. 10(a). The shock which is in the lower region of the reversing layer at maximum must move outward as time progresses, becoming lower in amplitude as it moves out (HW). Velocities from Shinkawa's red plates show a discontinuous change of smaller amplitude than the IR plates but at nearly the same phase – if anything, they shift velocity earlier. Also our plate shows two distinct components for which $\Delta v = 13\,\mathrm{km\,s^{-1}}$. To account for that shift we can let the shock pass through the region forming the lines observed in the blue and red plates at phase 0.9 to 1.1. Since a new shock is already beginning to emerge in the lower atmosphere at phase 0.9, this leads to the four-component two-shock model once again (Fig. 10b). Alternatively, we could assume that the lines on the 'red' plates (and the peaks labelled C and D in Fig. 8) are formed well above and well below the single shock, as sketched in Fig. 10(c); this does not make sense in terms of the expected relative transparency, however; it fails to explain why the C and D components are so clearly present in the histogram of Fig. 8; and it is also inconsistent with the regression coefficients for our plate and the progression of the dependence of v on χ_e in Shinkawa's Fig. 16.

5.5 CONCLUSION

For S Car, as for the other stars analysed, the two-shock model gives reasonable mass and radius and explains in a consistent manner the behaviour of the various components over the cycle.

6 Z Oph

This 350 day high velocity Mira variable is bluer and of earlier spectral type than the low velocity 300–400 day Miras; in these respects it more nearly resembles the shorter period (~ 150 day) Mira variables (Barnes 1973; Keenan 1966). This has led to the suggestion that Z Oph is the only fundamental mode Mira and that its 'normal, overtone' period would be 150 day (Barnes 1979, private communication). However, if the other Miras are already pulsating in the fundamental mode, as HW argued, an alternative explanation for Z Oph's idiosyncrasies must be found.

In this section we will show that the hypothesis that Z Oph is pulsating in a lower order mode (with larger Q) than either (a) the other 350-day Miras or (b) the 150-day Miras (represented by o Ceti and S Car respectively) is inconsistent with the observed velocity structure. We will then argue that all the anomalous properties of Z Oph can be explained on the relatively simple hypothesis that its atmosphere (as well as the atmospheres of the short period Miras) is more transparent in the visual than the atmospheres of the longer period, younger Miras.

The histograms for the plates of Z Oph are shown in Fig. 12. These show greater scatter than do the corresponding plots for RT Cyg and S Car; this will lead to greater uncertainty in the derived 'model' mass and radius for Z Oph.

6.1 FOUR-COMPONENT ANALYSIS

The interpretation of the regression analysis for Z Oph is similar to the interpretations for S Car and RT Cyg: cases a, c evolve towards d, b as the cycle progresses. In the case of

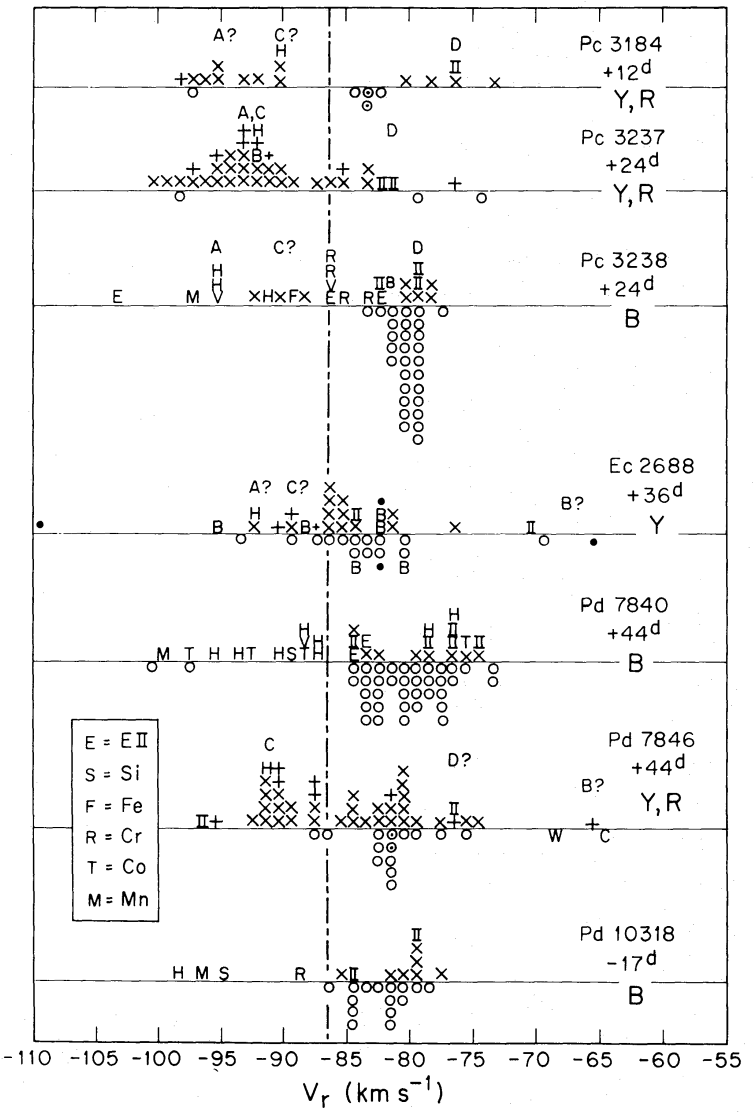

Figure 12. Histograms for the Z Oph plates.

Z Oph, where our last plate is at phase 0.13, case b is not yet seen but case d dominates the last few plates – as indeed the form of the histograms suggests it must.

Thus for Z Oph we see a progression from lines being formed in front of (falling into) a shock at $t = -17$ day to lines formed behind and across a shock, with the shock affecting first the high excitation lines (e.g. on plates Pc3237, 3238) and later the low excitation lines (e.g. Pc7840).

As for RT Cyg and S Car, the histograms reveal greater complexity than this simple picture. Proceeding as for those stars, we assign $v_* = -86\ \mathrm{km\ s^{-1}}$ and proceed to identify the shock components A to D in Fig. 12. Due to the relatively small number of lines and the relatively larger scatter the numbers of clearly determined components are few. There are three plates on which D components can be assigned with a degree of confidence; one ion line and scattered other features suggest the existence of component B but do not clearly place it; there are possible A components on several plates, but the only plate with a large number of substantially blueshifted lines is Pc3237, and there it is not clear whether a C component may not be blending with the A component.

Aggregating these tentative components near maximum we find for the amplitudes of the

two shocks

$\Delta v(0) \simeq 1.3 \times 23 \simeq 30\,\mathrm{km\,s^{-1}}$,

$\Delta v(P) \simeq 11\,\mathrm{km\,s^{-1}}$.

As we found for RT Cyg, the upper shock is shifted with respect to the stellar velocity defined by the lower; following the procedure used for RT Cyg and S Car we shall use the amplitude of the upper shock, rather than the velocity difference between the C component and the stellar centre of mass velocity derived from the A, B components, to estimate $v_0(P)$.

The best determined components are shown in Fig. 13 together with the curve for $c = 3$, $v_0(0) = 9\,\mathrm{km\,s^{-1}}$ which agrees adequately with these components. Other significant features of the histograms are sketched in, without geometrical correction, for reference. The mass radius plot for Z Oph is shown in Fig. 14, with lines of constant $v_0(0) = 8, 9\,\mathrm{km\,s^{-1}}$, $v_0(P) = 5\,\mathrm{km\,s^{-1}}$ and $Q = 0.1$, 0.15 day. (We have indicated the larger Q as well since Z Oph's unique status as an early-type Mira for its period may imply that its interior is significantly different from the structure of the models from which $Q \simeq 0.1$ day was derived. The observed velocities are consistent with Z Oph having a radius between 1.0 and 1.5×10^{13} cm and a mass between 0.5 and $1\,M_\odot$ for the indicated range of Q values.

As confirmation that $c = 3$ is reasonable for Z Oph the angular diameter variation of Z Oph from observed $V-R$ colours on three occasions near maximum (Barnes 1973) has been converted to angular diameters using the same F_V relation invoked above for RT Cyg. The two points at phase 0.06, 0.13 can be fit with $\phi(t)$ corresponding to $c = 3.8$, if $t = 0$ is taken at phase 0.06. We thus verify that $c = 3$ will work for Z Oph if the increase in ϕ_{V-R}

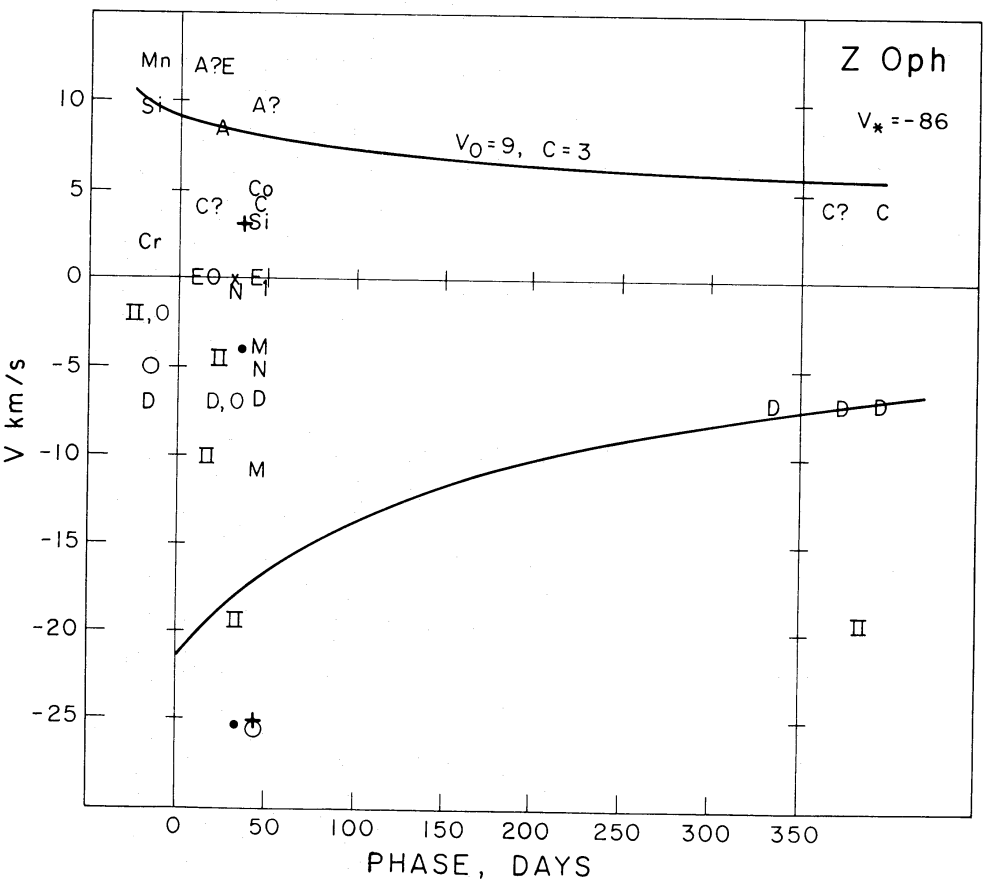

Figure 13. Velocity versus phase plot for Z Oph, comparing observed components with theoretical predictions.

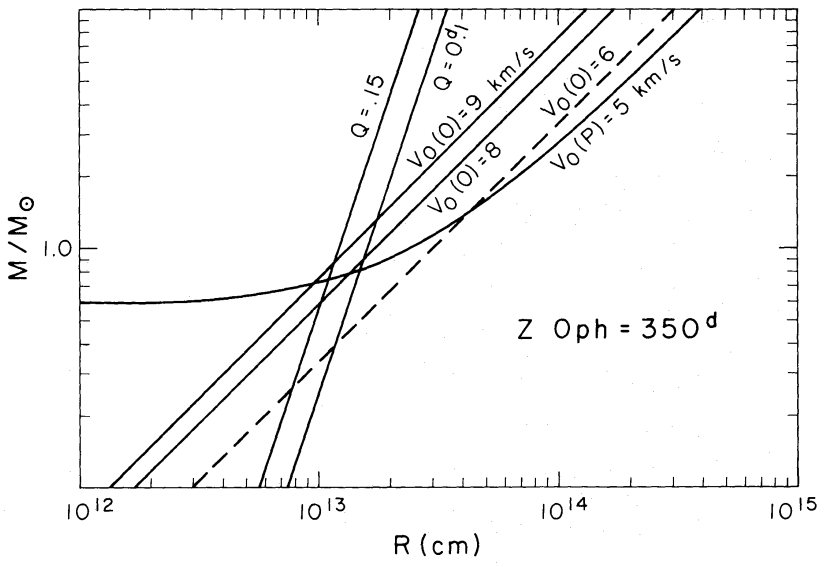

Figure 14. Mass versus radius for Z Oph.

from phase 0.06 to 0.13 is attributed to the a rising shock front; as noted for RT Cyg, earlier t_0 would give larger c.

6.2 PLATE-BY-PLATE ANALYSIS

To check these results for consistency, an alternative approach was tried: each plate was separately analysed for its two principal components, and these two components were then interpreted as being due to a single, photospheric shock. This was also motivated by the idea that Z Oph's uniqueness could be related to its having an (unobserved) companion, close enough for mass exchange to have occurred in the past. This approach led to a lower amplitude for the photospheric shock ($\Delta v = 20\,\mathrm{km\,s^{-1}}$ or $v_0(0) \simeq 6\,\mathrm{km\,s^{-1}}$) plus a shift from year to year in the deduced centre of mass motion

1957 (phase +12 to +24 day) $v_* = -89 \pm 1\,\mathrm{km\,s^{-1}}$,

1964 (phase +33 to +44 day) $v_* = -84 \pm 1\,\mathrm{km\,s^{-1}}$,

1967 (phase −17 day) $v_* = -89\,\mathrm{km\,s^{-1}}$.

The amplitude and period of the centre of mass motion implied by this interpretation are about right for a $0.5\,M_\odot$ companion located approximately 10 AU from the star itself.

This interpretation, while internally consistent, gives unlikely values for M and R. The line $v_0(0) = 6\,\mathrm{km\,s^{-1}}$ in Fig. 14 gives reasonable masses (0.5–$1\,M_\odot$) only for very small Q, large R. This is inconsistent with Z Oph's relation to both the short period high velocity Miras and to the other 300–400 day ones, as we shall show in more detail in the next section. We therefore doubt that Z Oph has such a companion.

6.3 NORMAL AND ABNORMAL PROPERTIES OF Z OPH

In Fig. 15 we show the mean $V-R$ at maximum versus $\log P$ for M type Miras, S type Miras, carbon star Miras and Z Oph using data from Barnes (1973). Clearly Z Oph differs either in period (from the short period stars) by a factor $P_Z/P_{150} \simeq 2.3$ or in colour (from the other 350 day stars) by $\Delta(V-R) \simeq 1.25$ in the sense that Z Oph is abnormally blue. Similar devia-

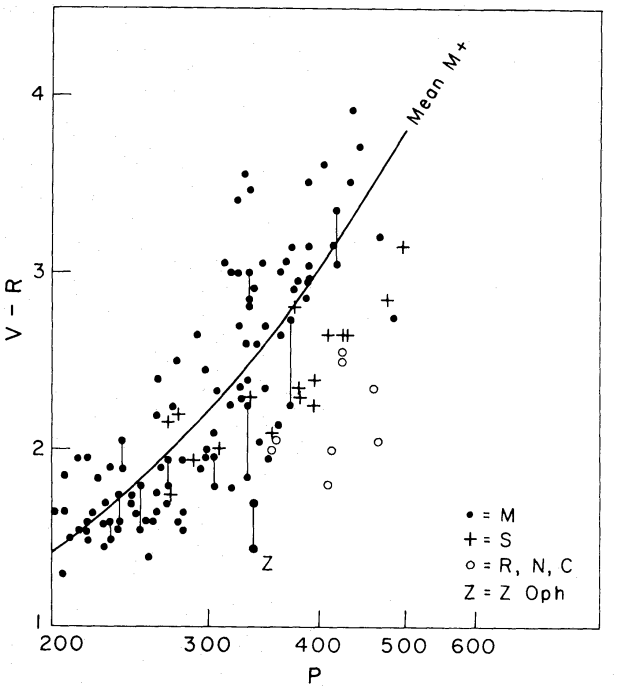

Figure 15. $V-R$ versus $\log P$ from Barnes (1973) for LPVs of spectral types K, M(•), S(+), and R, N, or C(○) with the location of Z Oph indicated (Z).

tions are found in other colours and in spectral type. However, it is also interesting to note that there are intermediate cases in the plot of $V-R$ versus P; in particular the carbon stars, whose atmospheric opacity might be expected to be significantly different from that of the M types, lie between the M type colour–period relation and the location of Z Oph.

In this section we will compare Z Oph to two other stars which we have studied using the same velocity analysis techniques: *o* Ceti, $P = 332$ day (from HW) and S Car, $P = 150$ day, from this paper. We shall seek to answer the question 'is Z Oph pulsating in the same mode or a higher or lower order mode than S Car or *o* Ceti?' The velocity data will be shown to strongly suggest the same mode for these three stars. In the last section we shall then show that all the observed 'abnormalities' of Z Oph can be expalined on the simple hypothesis that Z Oph differs from the younger 300–400 day Miras only in the relative transparency of its atmosphere.

6.3.1 Z Oph versus o Cet

The velocity analysis for Z Oph gave $v_0(0) \lesssim 9\,\mathrm{km\,s^{-1}}$, $c = 3$, while the corresponding analysis for *o* Cet (HW) gave $v_0(0) \simeq 10\,\mathrm{km\,s^{-1}}$, $c = 3$. Writing $v_0 = \beta v_e \propto \beta\sqrt{M/R}$, $c \propto \beta Q$ and $Q \propto P\sqrt{\rho} \propto P\sqrt{M/R^3}$ gives at once for any two stars A and B

$$\frac{V_{0A}}{V_{0B}} = \frac{c_A}{c_B}\frac{P_B}{P_A}\frac{R_A}{R_B}. \tag{13}$$

Hence for Z Oph and *o* Cet we have

$$\frac{R_Z}{R_o} = \left(\frac{9\,\mathrm{km\,s^{-1}}}{10\,\mathrm{km\,s^{-1}}}\right)\left(\frac{3}{3}\right)\left(\frac{350\ \mathrm{day}}{332\ \mathrm{day}}\right) = 0.95\,.$$

Thus Z Oph and *o* Cet are essentially the same size.

Further manipulation then gives

$$\frac{Q_o}{Q_Z} = \frac{P_o}{P_Z}\left(\frac{R_Z}{R_o}\right)^{3/2}\left(\frac{M_o}{M_Z}\right)^{1/2} = 0.88\left(\frac{M_o}{M_Z}\right). \tag{14}$$

This means that if *o* Cet were pulsating in an overtone and Z Oph in the fundamental ($Q_Z \gtrsim 2.5Q_o$) the mass of Z Oph would have to be more than five times larger than the mass of *o* Cet. This is clearly in contradiction to the hypothesis that Z Oph is an F mode counterpart to the low mass, short period LPVs.

We therefore conclude that Z Oph and *o* Cet are pulsating in the same mode.

6.3.2 S Car versus Z Oph

For both S Car and Z Oph we have found $c \simeq 3$ to give reasonable results; since $c \propto \beta Q$ we can write

$$\frac{\beta_Z}{\beta_S} = \frac{C_Z}{C_S}\frac{Q_S}{Q_Z} = \left(\frac{M_S}{M_Z}\right)^{1/2}\left(\frac{R_S}{R_Z}\right)^{-3/2}\left(\frac{P_S}{P_Z}\right)\left(\frac{C_Z}{C_S}\right). \tag{15}$$

Then from the definition of β

$$\frac{\beta_Z}{\beta_S} = \left(\frac{M_Z}{M_S}\right)^{-1/2}\left(\frac{R_Z}{R_S}\right)^{1/2}\frac{V_{0Z}}{V_{0S}}. \tag{16}$$

Combining these two expressions with $V_0 = 10\,\mathrm{km\,s^{-1}}$, $V_0 = 9\,\mathrm{km\,s^{-1}}$ gives

$$\frac{R_Z}{R_S} = \left(\frac{C_S}{C_Z}\right)\left(\frac{P_Z}{P_S}\right)\left(\frac{V_{0Z}}{V_{0S}}\right) = \left(\frac{3}{3}\right)\left(\frac{350\ \mathrm{day}}{150\ \mathrm{day}}\right)\left(\frac{9}{10}\right). \tag{17}$$

Substituting this into the expression for Q leads to

$$\frac{Q_S}{Q_Z} \approx 1.3\left(\frac{M_S}{M_Z}\right)^{1/2}. \tag{18}$$

If Z Oph is to be interpreted as the fundamental mode counterpart to S Car then the Q ratio must be $Q_S/Q_Z = 1/2.5$ which implies $M_Z \approx 10M_S$. This implies either an enormous mass for Z Oph or an impossibly small one for S Car. Another way to express this: if we assume that Z Oph and S Car must have comparable masses (within a factor of 2) we find

$$1.08 \geqslant Q_Z/Q_S \geqslant 0.54 \tag{19}$$

or, again, Z Oph and S Car are most likely pulsating in the same mode.

6.4 INTERPRETATION AND CONSEQUENCES OF THE COLOUR AND SPECTRAL TYPE ANOMALIES

We have shown that the hypothesis that Z Oph is the only F-mode pulsator among the LPVs is inconsistent with the velocity observations. In this section we will examine the alternative hypothesis, that it is the colour that is anomalous for Z Oph.

The angular diameters of LPVs which are determined by a variety of techniques seem to vary as a function of the wavelength interval being used (Wing 1979). Thus Labeyrie *et al.* (1977) found angular diameters for *o* Cet and R Leo that were smaller by a factor of 2 in continuum bands compared with their size in the TiO bands. The continuum determination

for *o* Cet, assuming a distance ~ 80 pc, gives a radius of ~ $250R_{\odot}$. Assuming a luminosity for *o* Cet of $6000L_{\odot}$ then gives an effective temperature of 3200 K – considerably hotter than the 2000–2800 K temperatures found from Johnson's (1966) $T_{\rm eff}$ calibrations for non-variable giants together with observed colours. Recent recalibrations of $T_{\rm eff}$ versus $(V-K)$ by Ridgway *et al.* (1980) give higher effective temperatures ($\geqslant$ 3000 K) for the giants but do not include any stars as red as the Miras. In comparison Z Oph's colour temperature ($V-R$ using Johnson's (1966) calibration) is about 3300 K, which agrees with the temperature indicated by its spectral type near maximum. Hinkle (1978) found an excitation temperature for the photospheric zone in R Leo which was similar: between 3000 and 3500 K at post-maximum phases. This suggests the possibility that the photospheric temperatures of all the LPVs is $\gtrsim$ 3000 K.

The 'true' diameter of an LPV is also more likely to be measured in the infrared, near the flux peak, than in the visual region where broad band measures average over the formation region of both molecular bands (formed at ~ $2r_0$) and continuum (formed at ~ r_0). A lunar occultation diameter of U Ori by Ridgway, Wells & Joyce (1977) near 2 μm is consistent with the narrow band continuum diameter of *o* Cet: the angular diameter of ~ 15 arcmin combined with an estimated distance to U Ori of 300 pc (from its mean visual magnitude at maximum plus the statistical parallax results of Clayton & Feast 1969) gives a stellar radius ~ $200R_{\odot}$. Thus the continuum and the infrared measurements agree in placing the photospheres of LPVs at smaller radii and higher temperatures than has been previously estimated from photometry. This 'true' angular diameter may also be recovered from the Barnes–Evans relation (F_V versus $V-R$) at maximum light, presumably because the light in the V and R bands at that phase comes from a rising shock front emerging from the photosphere at that phase (Barnes & Wilson 1981 in preparation).

Photometric properties of Z Oph and *o* Cet are summarized in Table 6. Due to its anomalous colours the absolute magnitude of Z Oph in these colours is very uncertain, and hence its distance is unknown. In order to find at least a first order reddening correction for

Table 6. Photometric properties of Z Oph and *o* Cet.

		Z Oph		*o* Cet
Property	Ref.	$A_V = 0$	$A_V = 1$	$A_V = 0$
$\langle m_v \rangle^{\rm max}$	1	8.1	7.1	3.3
$\langle m_{1.04} \rangle^{\rm max}$	2	5.0	4.5	– 1.4
$\langle m_K \rangle_{\rm mean}$	3	4.1	4.0	– 2.4
BC_K	4, 5	2.65	2.3	3.3
$m_{\rm bol}$		6.75	6.3	0.9
$(V-R)_{\rm max}$	6	1.4	1.1	$\gtrsim$ 2
$S_{\rm p}(V-R)$	4	M2.5	K4	$\geqslant$M4 5
$T_{\rm eff}(V-R)$	4	3500	4000	$\leqslant$ 3000
ϕ_{V-R}	7	1.0	1.0	24
$(J-K)_{\rm mean}$	3	1.0	0.83	1.2
$S_{\rm p}(J-K)$	4	M0.5	K3$^+$	$\gtrsim$ M6
$T_{\rm eff}(J-K)$	4, 5	3600	4200	$\lesssim$ 2800
Observed Sp. (max)	8	K3ep		M5.5e
$\Delta m_{\rm V}$		4.7		5.6
$\Delta m_{1.04}$		1.0		1.6
$\Delta m_{\rm K}$		$\gtrsim$ 0.65		$\gtrsim$ 0.89

References: 1 – GCVS (Kukarkin *et al.* 1969); 2 – Lockwood (1972); 3 – Catchpole *et al.* (1980); 4 – Johnson (1966); 5 – Robertson & Feast (1981); 6 – Barnes (1973); 7 – Barnes *et al.* (1978); 8 – Keenan (1966).

Z Oph we note that the distance estimates determined from its apparent magnitudes in V, $I(1.04)$, K and m_{bol} range from 750 to 2000 pc; at a galactic latitude of 21° this suggests a value of A_V between 0.4 and 1.0 mag. Rather than assuming that A_V is known, then, the magnitudes and colours in Table 6 are given for $A_V = 0.0$, 1.0 for Z Oph. For *o* Cet, with a distance $\lesssim 100$ pc, the expected reddening has no effect on the quantities displayed in Table 6.

Angular diameters for these two stars near maximum have been derived from F_V versus $V-R$ as described in Section 4.5.2. Note that Z Oph is blue enough to fall on the portion of the Barnes–Evans relation which has been calibrated from angular diameters for non-variable stars, and *o* Cet near maximum is also blue enough that the uncertainty in the extrapolated relation for LPVs is not yet large. The diameter derived here from F_V versus $V-R$ near maximum light for *o* Cet is nearly the same as the angular diameter derived by Labeyrie *et al.* (1977) from an analysis of speckle interferometric diameters with a variety of narrow- and broad-band filters, and is also close to the value determined by Robertson & Feast (1981) from *JHKL* observations; it is far smaller than the broad band visual angular diameters usually quoted.

From the combination of apparent bolometric magnitudes and angular diameters we can derive effective temperatures for these two stars; we find 2800 K for *o* Cet and 3900 K for Z Oph, in excellent agreement with the temperatures derived from these stars' spectral types and colours.

The period–mean density relation may be used to constrain 'reasonable' relative sizes of Z Oph and *o* Cet

$$\frac{R_Z}{R_o} = \left(\frac{350\text{ day}}{332\text{ day}}\right)^{2/3}\left(\frac{M_Z}{M_o}\right)^{1/3}.$$

This ratio is 0.8 if $M_Z/M_o = 0.5$ and 1.0 if the masses are equal. Making use of the effective temperatures then gives $L_Z/L_o = 2.5$ ($M_Z = 0.5\,M_o$) to 4 ($M_Z = M_o$). Combining the relative luminosities with the apparent bolometric magnitudes then tells us the relative distances must be 15 (mass ratio 0.5) to 20 (equal masses). Finally, the observed angular diameters combined with these distances give $R_Z/R_o = 0.6$ to 0.8. That is: if Z Oph and *o* Cet are pulsating in the same mode, consistency with the photometric properties of these two stars is obtained with Z Oph being less massive, slightly smaller, significantly hotter and more luminous than *o* Cet. (A similar analysis with the assumption that $Q_Z/Q_o \gtrsim 2$ would give $R_Z/R_o \lesssim 0.5$, $L_Z \sim L_o$, and a distance ratio $d_Z/d_o \lesssim 12$ to 15.)

6.5 SUMMARY

The masses and radii of the three stars analysed in this paper, together with three stars of younger population/longer period analysed previously (HW; Wallerstein 1979; Willson 1979) are shown in Fig. 16. Wallerstein (1979) found the difference between emission line and

Table 7. Density structure for $1\,M_\odot$ models. H_D is the dynamic scale height $H_0 + \beta^2 R$; $T = 3000$ K is assumed for all models.

θ	$R\,(10^{13}$ cm)	β	r_{us}/r_{ls}	H_D/R	ρ_{us}/ρ_{ls}
0.15	1.2	0.2	3.1	0.06	1.3×10^{-15}
0.10	1.6	0.2	2.5	0.07	3.8×10^{-10}
0.035	3.2	0.2	1.6	0.10	2.2×10^{-3}
0.035	3.2	0.4	2.1	0.22	1.4×10^{-5}

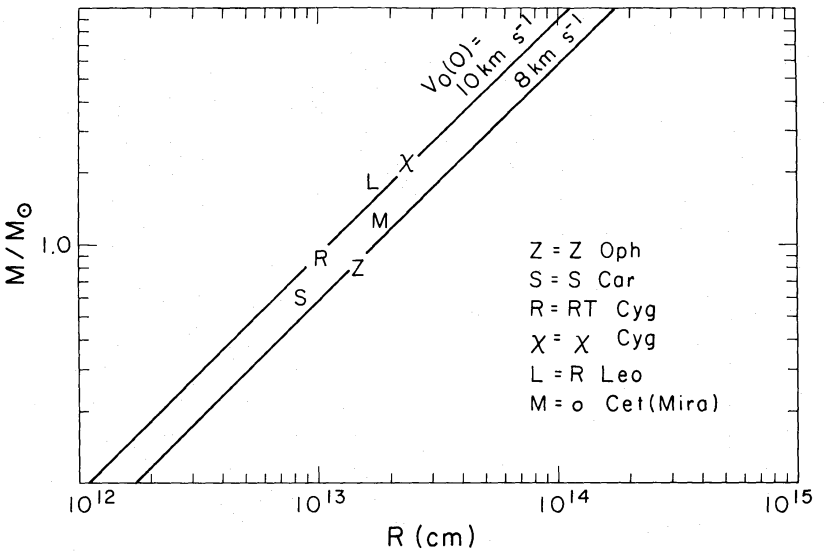

Figure 16. Combined mass–radius plot for the three Population II Miras considered in this paper plus three previously studied younger Miras (HW; Willson 1979). The diagonal lines represent $v_0(0) = 8$, $10\,\mathrm{km\,s^{-1}}$ as limits of $1.3(c - em) = v_0(0)$ for eight LPVs and S Per since the emission line velocity near maximum minus the systemic velocity appears to be constant (Wallerstein 1979).

centre of mass velocities for eight LPVs whose centre of mass velocities were determined by SiO thermal emission to lie between 6.2 and $8.0\,\mathrm{km\,s^{-1}}$ near maximum light. Multiplying these values by a geometrical correction factor $p = 1.3$ gives 8 to $10\,\mathrm{km\,s^{-1}}$ for the rising post-shock region that presumably produces that emission. The mass versus radius lines for $v_0(0) = 8$, $10\,\mathrm{km\,s^{-1}}$ are also indicated in Fig. 16; they can be seen to be consistent with the general location of the individual stars studied here. It is reassuring to note that the mean mass of the Population II Miras studied here is $\sim 0.8 M_\odot$ while the mean of the younger group (with $\langle P \rangle = 351$ day) is $\sim 1.8 M_\odot$ which is entirely consistent with Feast's (1962) analysis of the Mira main sequence progenitor masses. Our velocity analysis thus generally supports fundamental mode pulsation for the Miras, including S Car (150 day) and the anomalously K type ($P = 350$ day) Mira star Z Oph.

Acknowledgments

We would like to acknowledge the support of the National Science Foundation in the form of grants AST-7612162 (to LAW) and AST-7820405 (to GW). Also thanks are due to the staffs of the Dominion Astrophysical Observatory and Hale Observatories for telescope time and assistance. One particularly important spectrogram of RT Cyg, DAO 12199, was kindly obtained by M. Fletcher. Further assistance in data reduction was given by J. N. Pierce and D. Peterson of E. W. Fick Observatory. We are pleased to thank the referee for his incisive and constructive comments. No paper on LPVs is complete without an acknowledgment to Janet Mattei and the AAVSO without whose light curves and dates of maximum our observations would be uninterpretable.

References

Baade, W., 1963. *Evolution of Stars and Galaxies,* Harvard University Press, Cambridge.
Barnes, T. G., 1973. *Astrophys. J. Suppl.*, **25**, 369.

Barnes, T. G. & Evans, D. W., 1976. *Mon. Not. R. astr. Soc.*, **174,** 489.
Barnes, T. G., Evans, D. S. & Moffett, T. J., 1978. *Mon. Not. R. astr. Soc.*, **183,** 285.
Catchpole, R. M., Robertson, B. S. C., Lloyd-Evans, T. H. H., Feast, M. W., Glass, I. S. & Carter, B. S., 1980. *SAAO Circ.*, **1,** No. 4.
Clayton, M. L. & Feast, M. N., 1969. *Mon. Not. R. astr. Soc.*, **146,** 411.
Davis, D. N., 1947. *Astrophys. J.*, **106,** 28.
Eddington, A. S., 1939. *The Philosophy of Physical Science,* MacMillan, New York.
Feast, M. W., 1962. In *Variable Stars in Globular Clusters and Related Systems,* ed. Fernie, J. D., Reidel, Boston.
Gorbatskii, V. G., 1961. *Soviet Astr.-AJ,* **5,** 192.
Hall, R. N. B., Hinkle, K. H. & Ridgway, S. T., 1979. *Proc. IAU Colloq. No. 46, Changing Trends in Variable Star Research.*
Hill, S. J. & Willson, L. A., 1979. *Astrophys. J.*, **229,** 1029(HW).
Hinkle, K. H., 1978. *Astrophys. J.*, **220,** 210.
Hinkle, K. H. & Barnes, T. G., 1979. *Astrophys. J.*, **234,** 548.
Johnson, H. J., 1966. *A. Rev. Astr. Astrophys.*, **4,** 193.
Keenan, P. C., 1966. *Astrophys. J. Suppl.*, **118,** 333.
Kukarkin, B. V. *et al.*, 1969. *General Catalogue of Variable Stars,* 3rd edn, Moscow.
Kukarkin, B. V. *et al.*, 1976. *Third Supplement to the G.C.V.S.*, Moscow.
Labeyrie, A., Koechlin, L., Bonneau, D., Blazit, A. & Foy, R., 1977. *Astrophys. J.* (Letters), **218,** 427.
Lockwood, G. W., 1972. *Astrophys. J. Suppl.*, **24,** 375.
Maehara, J., 1968. *Publs astr. Soc. Pacif.*, **20,** 77.
Merrill, P. W., 1940. *The Spectra of Long Period Variable Stars,* Chicago University Press.
Merrill, P. W., Deutsch, A. J. & Keenan, P. C., 1962. *Astrophys. J.*, **136,** 21.
Merrill, P. W. & Greenstein, J. L., 1958. *Publs astr. Soc. Pacif.*, **70,** 98.
Parsons, S. B., 1972. *Astrophys. J.*, **174,** 57.
Payne-Gaposchkin, C. & Whitney, C. A., 1976. *SAO Special Report 370.*
Pettit, E. & Nicholson, S. B., 1933. *Astrophys. J.*, **78,** 320.
Pilachowski, C., Wallerstein, G. & Willson, L. A., 1979. *Proc. 1978 Goddard Conference on Current Problems in Stellar Pulsation Instabilities* (PWW).
Ridgway, S. T., Wells, D. C. & Joyce, R. R., 1977. *Astr. J.*, **82,** 414.
Ridgway, S. T., Joyce, R. R., White, N. M. & Wing, R. F., 1980. *Astrophys. J.*, **235,** 126.
Robertson, B. S. C. & Feast, M. W., 1981. Preprint.
Shinkawa, D. H., 1973. *Astrophys. J. Suppl.*, **25,** 253.
Tsuji, T., 1971. *Publs astr. Soc. Japan,* **23,** 275.
Wallerstein, G., 1979. *Proc. IAU Colloq. No. 46, Changing Trends in Variable Star Research.*
Willson, L. A., 1976. *Astrophys. J.*, **205,** 172.
Willson, L. A., 1979. *Proc. IAU Colloq. No. 46, Changing Trends in Variable Star Research.*
Wing, R. F., 1979. *Proc. 1978 Goddard Conference on Current Problems in Stellar Pulsation Instabilities.*
Wood, P. R., 1975. *Mon. Not. R. astr. Soc.*, **171,** 15P.